Performance Assessment of Optical Satellite-Based Operational Snow Cover Monitoring Algorithms in Forested Landscapes

Arnab Muhuri , Simon Gascoin , Lucas Menzel, Tihomir S. Kostadinov , Adrian A. Harpold,
Alba Sanmiguel-Vallelado, and Juan I. López-Moreno

Abstract—Forest cover is a crucial factor that influences the performance of optical satellite-based snow cover monitoring algorithms. However, evaluation of such algorithms in forested landscapes is rare due to lack of reliable *in situ* data in such regions. In this investigation, we assessed the performance of the operational snow detection (SCA) and fractional snow cover estimation (FSC) algorithms employed by the Copernicus Land Monitoring Service for High-Resolution Snow & Ice Monitoring (HRSI) with a combination of Sentinel-2 and Landsat-7/8 satellite scenes, lidar-based, and *in situ* datasets. These algorithms were evaluated over test sites located in the forested mountainous landscape of the Pyrenees in Spain and the Sierra Nevada in the USA. Over the Pyrenees site, the effectiveness of snow cover detection was evaluated with respect to a time-series of *in situ* snow depth measurements logged over test plots with different aspects, canopy cover, and solar irradiance. Over the Sierra Nevada site, the impact of ground vegetation was assessed over the under canopy fractional snow cover retrievals using airborne lidar-derived fractional vegetation cover information. The analyses over the Pyrenees indicated a good accuracy of snow detection with the exception of plots with either dense canopy cover or insufficient solar exposure (shaded forested slope), or both. The operational HRSI algorithm yielded similar performances (25–30% RMSE) as the computationally intensive spectral unmixing approach while retrieving the subcanopy ground FSC over the Sierra Nevada site. It was observed that a more accurate lidar-derived tree cover density map did not improve the subcanopy FSC retrievals.

Index Terms—Fractional snow cover area (fSCA), lidar, normalized difference snow index (NDSI), operational snow cover monitoring, snow cover area (SCA), tree cover density (TCD), under canopy snow cover.

Arnab Muhuri is with the Professorship in Hydrology and Climatology, Institute of Geography, Heidelberg University, 69120 Heidelberg, Germany, and also with the Centre d'Etudes Spatiales de la Biosphère (CESBIO) CNES/CNRS/INRAE/IRD/UPS, Université de Toulouse, 31000 Toulouse, France (e-mail: arnab.muhuri@alumni.uni-heidelberg.de).

Simon Gascoin is with the Centre d'Etudes Spatiales de la Biosphère (CESBIO) CNES/CNRS/INRAE/IRD/UPS, Université de Toulouse, 31000 Toulouse, France (e-mail: simon.gascoin@cesbio.cnes.fr).

Lucas Menzel is with the Professorship in Hydrology and Climatology, Institute of Geography, Heidelberg University, 69120 Heidelberg, Germany (e-mail: lucas.menzel@uni-heidelberg.de).

Tihomir S. Kostadinov is with the Department of Liberal Studies, California State University San Marcos, San Marcos, CA 92096 USA (e-mail: tkostadinov@csusm.edu).

Adrian A. Harpold is with the Department of Natural Resources and Environmental Science, University of Nevada, Reno, NV 89557 USA (e-mail: aharpold@cabnr.unr.edu).

Alba Sanmiguel-Vallelado and Juan I. López-Moreno are with the Department of Geoenvironmental Processes and Global Change, Pyrenean Institute of Ecology, 50059 Zaragoza, Spain (e-mail: albasv@ipe.csic.es; nlopez@ipe.csic.es).

Digital Object Identifier 10.1109/JSTARS.2021.3089655

I. INTRODUCTION

TERRESTRIAL snow cover is a crucial component of the global hydrological cycle and strongly influences net radiation balance [1]. A significant percentage of Earth's snow-covered regions are vast and geographically remote. Earth observation satellites have therefore been employed in such regions for monitoring the state of the global snow cover as early as the 1960s [2]. Among the different variables that can be effectively retrieved from the Earth observation satellites, snow cover information [quantified by either binary snow cover area (SCA) or fractional snow cover area (FSC/fSCA)] derived from the multispectral optical data is the most widely used [3]. In mountainous regions, snow cover extent information has been employed for driving hydrological forecasting models for early planning and management of winter precipitation, which is later released during the spring melt phase [4], [5]. Over a boreal forest landscape, fSCA derived from the MODIS data under an operational framework indicated improvement in the streamflow forecasts [6]. Moreover, the retreating extent of snow cover is considered as one of the primary indicators of global climate change [7]. Furthermore, the planetary snow and ice cover has a strong influence on the local and global albedo and participates in an important positive climate feedback process (ice-albedo feedback) [8]. Therefore, global SCA trend detection and quantification is important and requires operational monitoring on a regular basis. Monitoring of snow cover extent is also important for road authorities or winter tourism planning. A user survey in the recent past indicated the need for operational snow cover extent products with low latency (less than 12 h from the time of satellite acquisition) and high spatial resolution (better than 50 m) [9].

Optical sensors are reliable instruments for observing snow from space. The distinctly high reflectance of snow in the visible (VIS: 520–600 nm) and its highly absorptive nature in the shortwave infrared (SWIR: 1550–1750 nm) wavelengths of the electromagnetic spectrum are captured by multispectral sensors [10]. Such properties form the basis of the classical snow identification technique known as the normalized difference snow index (NDSI) [11], which combines VIS and SWIR channels and was documented several decades ago [12], [13]. However, NDSI only partly addresses the crucial issue of discriminating snow-covered land against other classes like vegetation. Therefore, the performance of this index remains rather questionable in forested landscapes, particularly due to the evolution of mixed pixel scenarios with varying snow, vegetation, and/or soil conditions [14]. Apart from the absence of sunlight and the presence of cloud cover, the overlying forest canopy limits the observation of snow cover with optical satellites [15], [16]. The degradation in the performance of this classical approach is caused by the overlying canopy volume. Such forest components present an obstruction and absorbs both the downwelling solar irradiance reaching the snow covered forest floor as well as the reflected upwelling radiance (the information-carrying signal). The degree of obscuration of the forest floor signal by the canopy elements is determined primarily by the tree cover density (TCD) [17], [18]. Thus, in addition to the varying snow cover fraction overlying the forest floor, the forest reflectance during winters is impacted by the fraction of sunlit snow visible through the canopy gaps or intercepted by the canopy [19]. Previous investigations have proposed spectral unmixing models to retrieve FSC from NASA's Moderate Resolution Imaging Spectroradiometer (MODIS). The endmember-model analyzes the surface reflectance data in the visible, near-infrared, and SWIR bands with multiple possibilities of spectral mixtures of endmembers like snow, vegetation, rock, and soil. The technique demands *a-priori* knowledge of the endmember spectra in the image or derivation of the spectra using a radiative transfer model [20], [21]. Endmembers may vary spatially and seasonally in forested areas due to processes like seasonal snowfall, litterfall, and shadow effects on the spectral albedo. Therefore, such detailed information when available is expected to provide a reliable estimate of the FSC. Such level of complexity is, however, processing-intensive. Furthermore, these factors are in contrast to the constraints like low latency and wide-areal coverage, which are essential for operational implementation of an Earth observation algorithm on a global scale. A recent assessment of the existing snow information retrieval techniques for the MODIS data revealed that the spectral unmixing-based algorithms did not outperform the NDSI-based approaches [22]. Despite the existing challenges, present investigations are striving to improve the state-of-the-art in spectral unmixing-based snow information retrievals (snow cover fraction, albedo, and grain size) from an operational point of view [20], [21], [23]. Although MODIS allows near-daily generation of the operational FSC maps at a wider spatial scale, its coarse spatial resolution (from 250 to 1000 m) and the requirement for additional compensation due to cumulative shielding effect of the forest canopy (obscuring the under canopy snow cover) with growing viewing zenith angle (VZA) (due to the oblique off-nadir viewing geometry of wide-swath systems) favors high-resolution sensors like Sentinel-2 and Landsat-8 [16], [21], [24]–[29].

With the possibility to process high-resolution Sentinel-2 and Landsat-7/8 multispectral optical datasets under the high-resolution snow & ice monitoring (HR-S&I) Let-It-Snow (LIS) framework of the Copernicus land monitoring service (CLMS), snow cover information (SCA and FSC) is now available at a spatially finer scale [30]. Although the top-of-the-canopy FSC (FSC_{TOC}) algorithm was already evaluated using multiple in situ and very high-resolution remote sensing datasets, the evaluation focused on the snow cover above the tree line, and, therefore, the effect of the canopy adjustment on on-ground FSC (FSC_{OG}) was not assessed [31], [32]. Moreover, the calibration and evaluation were performed over the European sites. Therefore, this investigation provides an opportunity to build upon the existing knowledge from the past analyses by further assessing the algorithms' performance in other regions to scrutinize the aspect of landscape diversity [22]. Furthermore, this evaluation is important for users of the HR-S&I service, particularly if the FSC products are to be assimilated into a snowpack model [33]. Due to the prevalence of mixed pixels in the forested landscapes, merely binarizing pixels into snow/snow-free can introduce errors while integrating the SCA information for hydro-climatological modeling [34]. The fSCA, which is a finer representation of the binary SCA and defines the snow-covered fraction of the pixel area, has been observed to improve estimations crucial for better modeling of land surface and hydrological regimes [35].

In this investigation, we assessed the performance of both the operational SCA detection and the subcanopy snow cover fraction (FSC_{OG}) retrieval algorithms over the forested landscapes. Such assessment is challenging given the limited detailed *in situ*/lidar-based observations of SCA and FSC under the forest canopies with near-overlapping cloud-free satellite data [36]. We exploited datasets from two recent investigations. One is a time-series of snow depth (SD) measurements logged during three consecutive winters in a forested valley located in the central Spanish Pyrenees mountain range [37]. This dataset enabled determination of the presence/absence of snow cover and hence was employed to evaluate the SCA algorithm. The other dataset was acquired in a forested terrain over the Sagehen Creek Watershed in the Sierra Nevada, CA, USA using multiple airborne lidar overflights (for vegetation fraction: 2014 and snow cover: 2016) and was postprocessed to determine the fractional vegetation and subcanopy snow cover fraction at high spatial resolution [38].

II. OPERATIONAL ALGORITHM

The recently launched HR-S&I service by the CLMS exploits high-resolution multispectral optical satellite data to produce operational snow cover maps, including top-of-canopy FSC (FSC_{TOC}) and on-ground FSC (FSC_{OG}), all based on the NDSI. The algorithms were designed to work equivalently with Landsat-7/8 and Sentinel-2 L2A products, which are surface reflectance values obtained after correction of atmospheric and

terrain effects (flat surface reflectance) including generation of a cloud and cloud shadow mask. The NDSI is derived from the flat surface reflectance data as shown in the following equation:

$$\text{NDSI} = \frac{\rho_{\text{Green}} - \rho_{\text{SWIR}}}{\rho_{\text{Green}} + \rho_{\text{SWIR}}} \tag{1}$$

where ρ_{SWIR} is the flat surface reflectance in the SWIR band at 1565–1655 nm (central wavelength: 1610 nm) and ρ_{Green} is the flat surface reflectance in the visible green band at 543–578 nm (central wavelength: 560 nm) for Sentinel-2 (Landsat-7 ETM+: 520–600 and 1550–1750 nm and Landsat-8: 530–590 and 1570–1650 nm, respectively, for the Green and SWIR bands).

The SCA detection algorithm is based on the NDSI with some additional criterion (like inclusion of red band reflectance and gap-filled digital elevation model from NASA's Shuttle Radar Topography Mission for elevation thresholding to minimize false snow detection) that enhances the robustness of snow detection [31]. The satellite data was atmospherically corrected to surface reflectance products (Sentinel-2 L1C to L2A) using the MACCS-ATCOR Joint Algorithm (MAJA) module, which demonstrated better performance with atmospheric correction and cloud detection benchmark studies [39]. MAJA is an operational module that takes into account time-series of satellite scenes to estimate the aerosol optical thickness and classify cloud pixels, which apart from correcting for the atmospheric haze also accurately resolves the snow-cloud ambiguity [40], [41]. The FSC_{TOC} is related to the NDSI by a sigmoid-shaped function, which was empirically established as shown in the following equation [32]:

$$\text{FSC}_{\text{TOC}} = \frac{1}{2}(\tanh(2.65 \times \text{NDSI} - 1.42) + 1). \tag{2}$$

A past investigation with the coarse-resolutioned MODIS data indicated a regression relationship between FSC and NDSI to be reasonably robust and applicable both on a local and continental scale [42]. The FSC_{TOC} is computed only for the pixels marked as snow-covered, determined by the SCA algorithm described above [31]. The FSC_{OG} is estimated by canopy adjustment of FSC_{TOC} as shown in the following equation [16], [25], [43], [44]:

$$\text{FSC}_{\text{OG}} = \min(\text{FSC}_{\text{TOC}}/\text{VGF}, 1) \tag{3}$$

where VGF is the viewable gap fraction, which is determined by the TCD as shown in the following equation:

$$\text{VGF} = 1 - \text{TCD}. \tag{4}$$

For VGF $= 0$, the algorithm returns $\text{FSC}_{\text{OG}} = 1$ when $\text{FSC}_{\text{TOC}} > 0$, whereas it returns $\text{FSC}_{\text{OG}} = 0$ when $\text{FSC}_{\text{TOC}} = 0$. When TCD is not defined or not available, $\text{FSC}_{\text{OG}} = \text{FSC}_{\text{TOC}}$ [30]. The TCD is adopted from the Copernicus Tree Cover Density (version 2015) [45] and resampled on the same grid as the L2A product using bilinear resampling (bilinear is preferred to the cubic method since the latter may result in values outside the range of the input map, i.e., beyond 0%–100%).

High-resolution multispectral optical satellite systems like Sentinel-2 (20 m) and Landsat-7/8 (30 m) acquire data at a significantly narrower swath widths (near-nadir viewing geometry), achieved with the pushbroom mode of image acquisition (as opposed to whiskbroom mode in MODIS), which eliminates the need for any pixelwise geometrical corrections with respect to the VZA. Although the computation of SCA and FSC at relatively higher spatial resolutions (as compared to MODIS) addresses the issue of mixed pixels to a certain extent, the influence of ground parameters like vegetation fraction still plays an important role in determining the performance of the NDSI-based algorithms [34], [46], [47]. This occurs since the varying topography and vegetation distribution controls the spectral signature of snow cover, canopy occlusion and shading, and topographic shadowing, which impact the NDSI [48]. Therefore, evaluation of the impact of such factors over the operational algorithms' performance is a crucial exercise.

III. Test Sites and Data

A. Test Site A: Pyrenees

This site is located in the Balneario de Panticosa valley in the central Spanish Pyrenees near the French–Spanish border, as shown in Fig. 1.

For a recent investigation, the site offered the opportunity to look into the spatial and temporal interactions of forests with snowpack accumulated over a range of site conditions [37].

The site is divided into four plots with each plot further segmented into forest opening (O) and beneath forest canopy (F) sections. The plots are located at varying altitudes, as shown in Fig. 1, and are further classified by their unique site characteristics like aspect, percentage canopy cover, solar irradiance, and several other factors (Table I).

1) In Situ Data:
1) SD: Daily SD data were logged over the test plots (P1, P2, P3, and P4) using a semiautomatic (since photographs were manually processed to extract SD) time-lapse cameras and snow pole setup [eight such pairs were divided over each plot with 3 in the forest openings (O) and 5 beneath the forest canopy (F)]. A random forest based regression technique was utilized to gap-fill the missing data at the snow poles [49]. The semiautomatic SDs were cross-validated with the manual SD measurements taken during field surveys conducted at an interval of 10–15 days. The measurements were taken from the onset of snow accumulation (in November) until the end of the melting season (in May/June) during the winters of 2015/2016, 2016/2017, and 2017/2018.
2) Site factors: The essential factors considered over this site are detailed in Table I. These factors can typically impact the satellite retrievals of snow cover information and also modify the snowpack characteristics [50]–[58]. The site is dominantly covered by mountain pine and Scots pine (*Pinus uncinata* Ram. and *Pinus sylvertris* L.), with each one prominently distributed at a different elevation range (mountain pine: from 1600 to 2500 m and Scots pine: from 1200 to 1900 m a.s.l.). This influences the degree of snowpack–forest interaction, which is known to also vary with the altitude (from 1600 to 2500 m a.s.l. for the Pyrenees) [57]–[61].

TABLE I
AVERAGE VALUES OF SITE CHARACTERISTICS OVER SITE A [37]. THE POTENTIAL SOLAR IRRADIANCE (PSI) AND OBSERVED SOLAR IRRADIANCE (OSI) ARE EXPRESSED AS $1000 {\wedge} * Whm^{-2}$ AND Wm^{-2}, RESPECTIVELY, AND BOTH ARE AVERAGED FROM MARCH TO MAY. UTM COORDINATES ARE IN ZONE: 30 N AND DATUM: WGS84

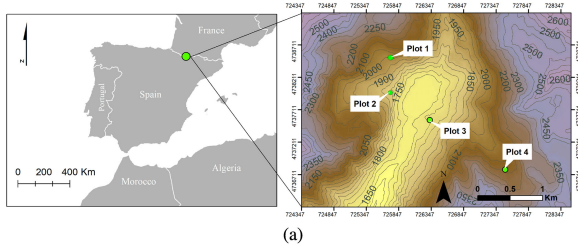| Plots	UTM Easting (m)	UTM Northing (m)	Elevation (m a.s.l.)	Aspect (degrees)	Canopy Cover (%)	PSI	OSI
P1 (Upper)	725,720	4,738,517	2008	S (193.66)	156	165.3	154.4
P2 (Lower)	725,718	4,737,976	1814	E (79.92)	85	129.6	167.6
P3 (Lower)	726,325	4,737,554	1674	W (261.7)	119	140.2	192.7
P4 (Upper)	727,488	4,736,790	2104	NE (48.3)	29	122.6	195.1

(a)

(b)

(c)

Fig. 1. Test Site A: Relative location of the test plots in the Balneario de Panticosa, Northeastern Iberian Peninsula, Central Spanish Pyrenees. UTM Zone: 30 N and Datum: WGS84. Figures are reproduced with permission from [37]. (a) Relative location of the test plots in the Balneario de Panticosa valley. (b) Relative location of the test plots: P1 and P2. (c) Relative location of the test plots: P3 and P4.

The percentage canopy cover referred to in Table I is the proportion of the forest floor covered by the vertical projection of the tree crowns [62]. For canopy cover estimation, two crown projections (one perpendicular and one parallel to the terrain slope line) were measured for each individual pine. Two area values were calculated from these measurements, which were then averaged. The cover area of each pine was then expressed as a percentage of the subplot area. Finally, all individual canopy cover percentages were aggregated. Canopy cover values can be higher than 100% since it aggregates (as the percentage of subplot area) the individual crown projections of the trees, which in some cases may overlap. The experimental setting composed of one plot of approximately 450 sq. m in each forest stand. The canopy cover, tree density, and basal area measurements were conducted over 15 × 15 m subplots, which is composed of approximately half of each studied plot [37], [62].

The site is divided into several plots (P1, P2, P3, and P4). Based on the elevation, the plots were broadly classified as either an "Upper (U)" or a "Lower (L)" plot. Apart from differences in their elevations, the plots were chosen in a manner that each one is facing a different cardinal/intercardinal direction. This is quantified by the aspect of the plot that determines if a slope is facing away from or directly toward the incoming solar irradiance. For slopes facing southwards, the exposure to solar irradiance is expected to be higher as compared to the northwards facing slopes.

However, the net irradiance received by an area is not only a function of its aspect but also depends on several other factors like percentage canopy cover. This can be appreciated in Table I for P1, which, due to its location, shows the highest "Potential Solar Irradiance." However, due to the sheltering effect of the high percentage canopy cover over P1 (the highest among all the plots), the "Observed Solar Irradiance" is the lowest. The observed irradiance is logged by an automatic weather station installed at the forest opening of each plot, whereas the potential irradiance is the calculated amount of radiant energy for a specific location and time period [37]. The values presented in Table I for both these irradiance measurements are averaged from March to May.

2) Satellite Data: Due to the daily long-term time-series *in situ* data acquisition plan over Site A, a significant number of high-resolution Sentinel-2 acquisitions were available temporally overlapping the ground data acquisitions. Therefore, the analysis over Site A exploited the large number of suitable acquisitions from the winters of 2016/2017 and 2017/2018 to compute the SCA ($FSC_{TOC} > 0$) using the MAJA-LIS workflow [31].
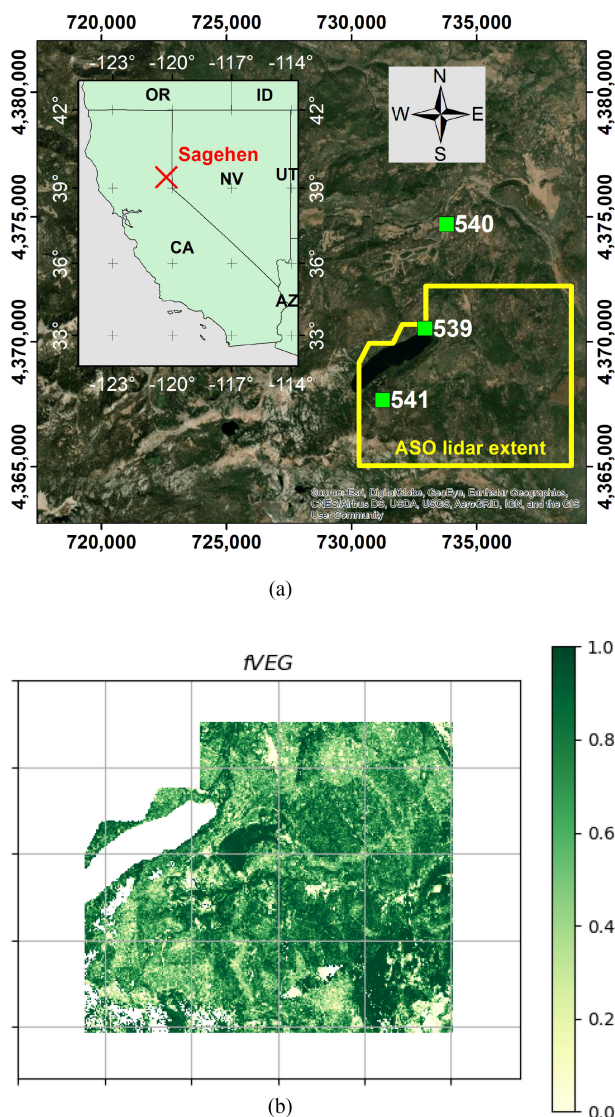
(a)

(b)

Fig. 2. Test Site B: Sagehen Creek Watershed, Northern Sierra Nevada Mountain Range, CA, USA. UTM Zone: 10 N and Datum: NAD83. Figures are reproduced with permission from [38]. (a) Location of the Sagehen Creek Watershed with Snow Telemetry (SNOTEL) stations (# 539, 540, and 541 denoted by the green squares) and NASA's Airborne Snow Observatory (ASO) footprint (enclosed by the yellow polygon). (b) NCALM 2014 snow-off lidar data derived fractional vegetation cover (fVEG) over the NASA's ASO lidar extent in Site B.

B. Test Site B: Sierra Nevada

This site is located in the Sagehen Creek Watershed in the northern Sierra Nevada, CA, USA, as shown in Fig. 2. The site footprint [denoted by the Airborne Snow Observatory (ASO) lidar extent] includes Lake Independence and other small water bodies, which are excluded from our analysis. The site is mostly covered by coniferous forests with trees of varying heights and canopy densities.

1) Lidar-Based Data: The fractional vegetation cover (fVEG) was derived from the airborne lidar dataset provided by the National Center for Airborne Laser Mapping (NCALM) [63], which was acquired during the summer of 2014

as a part of the Tahoe National Forest lidar survey. The NCALM 2014 snow-off lidar data essentially captured the vegetation heights. fVEG defines the fraction of tall canopy (NCALM vegetation heights greater than 2 m) at 10 m spatial resolution (composed of 1 m pixels) [38]. fVEG (lidar-derived) and TCD (multispectral satellite-derived [64]) are positively correlated indices quantifying the percentage abundance of canopy cover over a pixel. These indices are employed to investigate the impact of quality of vegetation fraction data, derived from different sources (airborne lidar and satellite) at different spatial scales, over the FSC_{OG} retrievals.

NASA's ASO was flown over the test site on March 26, April 17, and May 18, 2016 in order to acquire lidar measurements during the snow depletion phase of the season [65]. The estimation of fractional SCA (FSC_{REF} or fSCA as referred in [38]) at 10-m resolution over the test site involved combination of the fVEG information, derived from the NCALM snow-free lidar point cloud data, and the snow presence/absence information (at 1 m resolution), derived from the within-pixel mean lidar return elevation in the ASO data [38]. For additional details on lidar data processing and snow cover measurements over Site B, refer to [38].

2) Satellite Data: Due to the spatially distributed (high spatial density) nature of the airborne lidar measurements over Site B (also referred here as groundtruth), data from multiple high-resolution satellite platforms (S2 and L7/8) were integrated to demonstrate the optimal utilization of temporally overlapping (nearly coinciding in time) and spatially similar sensor (closely matching in spatial resolution) acquisitions.

1) Sentinel-2 (20 m): The Sentinel-2 scenes were processed to FSC_{TOC} and FSC_{OG} using the MAJA-LIS framework as performed operationally within the CLMS HR-S&I service. The processing was done offline as the area is not covered by the service yet (only Europe).

2) Landsat-7 ETM+ (30 m with SLC-Off) and Landsat-8 (30 m): After the Landsat-7 ETM+ (the predecessor of Landsat-8) experienced a scan line corrector (SLC) mechanism failure on May 31, 2003, the scenes exhibited wedge-shaped scan-to-scan gaps with no-data values as a result of the normal scanning pattern [66]. However, the L7 system with its SLC powered off is still able to acquire useful data by sacrificing approximately 22% of the scene's normal coverage. Despite the SLC failure, the scenes maintain the previous level of radiometric and geometric corrections. Although a range of gap-filling approaches are available to compensate for the issue of SLC failure, our analysis in this investigation was only performed over the native L7 pixels by masking the no-data areas [67].

Landsat offers multispectral satellite data like the Sentinel-2 but at a slightly coarser spatial resolution and a longer revisit time. However, in the absence of a Sentinel-2 satellite pass, the Landsat data can be utilized due to their comparable spatial resolutions (S2: 20 m and L7/8: 30 m). Moreover, the United States Geological Survey (USGS) Earth Explorer provides both Landsat-7/8 atmospherically corrected surface reflectance products. These products

were processed in a manner similar to the Sentinel-2 datasets with the LIS processor [31], [68].

3) USGS Landsat-Derived FSC (FSC_{TMSCAG}): The analysis-ready FSC maps were obtained from the USGS Earth Explorer, which are generated from the temporally coincident Landsat-7/8 datasets using the TMSCAG approach [20], [69]. TMSCAG is an adaptation of MODSCAG for Landsat ETM+ and TM data for FSC estimation [70].

4) Auxiliary Vegetation Map: Due to the absence of the Copernicus TCD map over this region (available only for Europe), the freely distributed global TCD map at 30 m spatial resolution (resampled for S2) was employed for canopy adjusting the FSC_{TOC} maps to $FSC_{OG: TCD}$ [64]. Although lidar-derived vegetation cover information (like fVEG) are desirable due to their higher spatial detailing, the satellite-derived TCD from multispectral data reliably fulfils this gap due to the lack of such high-resolution lidar products on a global scale, thus enabling rescaling of FSC for operational purposes. In order to assess the performance impact of high-resolution lidar-derived fVEG over the rescaled FSC_{TOC}, the airborne lidar data was employed to obtain the $FSC_{OG: fVEG}$ and compared with the $FSC_{OG: TCD}$.

IV. METHODOLOGY

Over Site A in the Pyrenees, the performance of satellite-based snow detection (binary SCA: snow/snow-free) was investigated with respect to the *in situ* time-series SD profile indicating presence/absence of snow cover. The performance was assessed with respect to varying site factors like forest cover, topography, and meteorological variations. Although a significant number of Sentinel-2 scenes were available overlapping the ground data acquisition period, the effective number of scenes suitable for analyses were reduced due to the obscuring effect of the cloud cover. Besides, Sentinel-2 data was not available during the winter of 2015/2016.

Over Site B in California, we analyzed the performance of the FSC (continuously varying from 0 to 1) algorithm and also looked at the performance of snow detection at different ranges of fVEG, as shown in Fig. 2(b). Due to the limited number of lidar data acquisition dates, a combination of the Sentinel-2 and Landsat-7/8 scenes (with minimum temporal gap between the lidar flights and satellite acquisitions) was employed to compensate for the cloud-cover and satellite revisit time.

The *in situ*/lidar-based data utilized in this investigation over the two sites are unique with respect to their applicability for the evaluation of the operational SCA and FSC algorithms.

1) Site A: Point-based *in situ* measurements observed over a temporally longer duration (2015/2016, 2016/2017, and 2017/2018) and compared with a significantly large number of satellite acquisitions (70 Sentinel-2 scenes).

2) Site B: Spatially distributed airborne lidar measurements (also referred here as groundtruth) observed over a temporally shorter duration (March 26, April 17, and May 18, 2016) and compared with limited number of satellite

TABLE II
CONFUSION MATRIX FOR BINARY CLASSIFICATION. G: GROUNDTRUTH AND S: SATELLITE. TP: TRUE POSITIVE, TN: TRUE NEGATIVE, FP: FALSE POSITIVE, AND FN: FALSE NEGATIVE. N = TP + TN + FP + FN. NORMALIZED CONFUSION MATRIX ELEMENTS: THE TP, FN, FP, AND TN ARE NORMALIZED BY DIVIDING EACH ONE OF THEM WITH THE SUM OF THE ELEMENTS IN THE CORRESPONDING ROW OF THE CONFUSION MATRIX. THE VARIATION OF THE NORMALIZED ELEMENTS IS CONSTRAINED BETWEEN 0 AND 1

		S		
		Snow	Snow-Free	Total
G	Snow	TP	FN	TP + FN
	Snow-Free	FP	TN	TN + FP
	Total	TP + FP	TN + FN	N

acquisitions (Sentinel-2 and Landsat-7/8) at high data point density.

Due to different spatial resolutions of the groundtruth (lidar-derived) and satellite-derived maps over Site B, the groundtruth maps were resampled (downsampled) to match the satellite resolution. The average resampling method was employed to avoid excessive smoothing [71]. The fVEG and the FSC_{REF} maps, derived from the airborne lidar measurements, were resampled from their native 10-m resolution to 20 m (in case of Sentinel-2) and 30 m (in case of Landsat-7/8).

In case of Site A, no such resampling was required due to the point-based nature of the measurements over the test plots (P1, P2, P3, and P4). The geographic coordinates for each plot were utilized to compare the satellite observations with the *in situ* measurements. Single pixel geographic coordinates of the plot centers (UTM coordinates) are as shown in Table I. These coordinates were employed for the analyses by assuming that the *in situ* data acquisition points were discretely located within a 20 × 20 m Sentinel-2 pixel.

A. Evaluation Metrics

1) Confusion Matrix Parameters: Snow cover detection can be considered as a binary classification problem where a pixel is either classified as snow-covered or snow-free. Confusion matrix is a means to evaluate performance of the algorithms involved in such classifications (but not limited to two classes) [72]–[74]. The confusion matrix for a binary snow/snow-free classification scenario is as shown in Table II.

The matrix quantifies both the correctly classified (pixel assigned to the original class) and misclassified (pixel assigned to the erroneous class) pixels. The original/erroneous class is determined from the *in situ*/lidar-based datasets (G) acquired over Site A and B.

The confusion matrix elements encapsulates the following information.

1) True Positive (TP): The TP defines those pixels which are verified by the in situ/lidar-based data as SNOW-COVERED and also identified from the satellite data (by the algorithms) as SNOW pixels.

2) True Negative (TN): The TN defines those pixels which are verified by the in situ/lidar-based data as SNOW-FREE and also identified from the satellite data as NO-SNOW pixels.

3) False Positive (FP): The FP defines those pixels which are verified by the in situ/lidar-based data as SNOW-FREE but identified from the satellite data as SNOW pixels.

4) False Negative (FN): The FN defines those pixels which are verified by the in situ/lidar-based data as SNOW-COVERED but identified from the satellite data as NO-SNOW pixels.

These matrix elements are further utilized to compute performance metrics for the satellite-based algorithms. These metrics are defined as follows.

1) Accuracy (Ac): The accuracy of an algorithm (also called observed accuracy, $\mathrm{Ac_{obs}}$) is defined as the rate of correct classification. In this expression, if the misclassification terms FP and FN are zero, then the accuracy of the algorithm will be 100%. The $\mathrm{Ac_{obs}}$ is computed as

$$\mathrm{Ac_{obs}} = \frac{\mathrm{TP} + \mathrm{TN}}{\mathrm{TP} + \mathrm{TN} + \mathrm{FP} + \mathrm{FN}}. \tag{5}$$

2) Cohen's Kappa Coefficient (κ): The Cohen's kappa coefficient (κ) is a relatively pessimistic measure of the algorithm's performance (a more robust measure as compared to $\mathrm{Ac_{obs}}$), particularly for an imbalanced dataset (if the extents of snow-covered versus snow-free areas are significantly different). It is a function of the observed accuracy ($\mathrm{Ac_{obs}}$) and the random/expected accuracy ($\mathrm{Ac_{rand}}$) [75]. A complete agreement with respect to the *in situ*/lidar-based data is indicated by $\kappa = 1$, whereas $\kappa = 0$ indicates merely a random agreement (an agreement by chance) [76]. κ is an important measure to be considered with $\mathrm{Ac_{obs}}$ since it attempts to remove imbalance/bias in the class distribution (one class is more prevalent than the other) and points out a disagreement if $\mathrm{Ac_{obs}}$ is less than the $\mathrm{Ac_{rand}}$ [77]. The coefficient of agreement kappa is defined as

$$\kappa = 1 - \frac{1 - \mathrm{Ac_{obs}}}{1 - \mathrm{Ac_{rand}}}$$
$$= \frac{\mathrm{Ac_{obs}} - \mathrm{Ac_{rand}}}{1 - \mathrm{Ac_{rand}}}$$
$$\mathrm{Ac_{obs}} = \frac{\mathrm{TP} + \mathrm{TN}}{\mathrm{N}}$$
$$\mathrm{Ac_{rand}} = \frac{(\sum R_1)(\sum C_1) + (\sum R_2)(\sum C_2)}{\mathrm{N}^2}$$
$$\sum R_1 = (\mathrm{TP} + \mathrm{FN})$$
$$\sum C_1 = (\mathrm{TP} + \mathrm{FP})$$
$$\sum R_2 = (\mathrm{TN} + \mathrm{FP})$$
$$\sum C_2 = (\mathrm{TN} + \mathrm{FN}).$$

2) Additional Metrics: Apart from the metrics derived from the confusion matrix, we computed the following statistical metrics to compare the degree of agreement between the observed and the estimated FSC (lidar-based and satellite data, respectively). Unlike for the binary SCA analyses where confusion matrix parameters were suitably employed, FSC is a continuously varying quantity (snow cover fraction varies continuously from 0 to 1), and, therefore, the following statistical measures were necessary for its evaluation.

1) Root Mean Square Error (RMSE): RMSE is a measure of the normalized distance between the observed and the predicted data samples. Here, RMSE is used to compare the observed (x_i) and the estimated (y_i) FSC. It is defined as

$$\mathrm{RMSE} = \sqrt{\frac{1}{n} \sum_{i=1}^{n} (x_i - y_i)^2}. \tag{6}$$

2) Pearson Correlation Coefficient (CC): CC is a measure that indicates the strength of the association (positively or negatively correlated) between the observed and the estimated FSC. It is defined as

$$\mathrm{CC} = \frac{\sum_{i=1}^{n}(x_i - \overline{x})(y_i - \overline{y})}{\sqrt{\sum_{i=1}^{n}(x_i - \overline{x})^2 \sum_{i=1}^{n}(y_i - \overline{y})^2}}.$$

B. Workflow

1) Over Test Site A: Confusion matrix analysis was employed to assess the performance of snow detection with time-series of Sentinel-2 acquisitions over Site A. The snow-covered/snow-free pixels were distinguished by thresholding the satellite-derived $\mathrm{FSC_{TOC}}$ (> 0). SD at each test plot was considered as a measure to determine the presence/absence of snow cover. Since SD was measured at both the open vegetation-free (O) and canopy covered (F) sections, the confusion matrix metrics were derived by comparing the thresholded satellite observations (binary SCA: snow/snow-free) with the SDs from both these sections. The confusion matrix elements for the initial iteration was computed for all SD > 0.1 cm. This *in situ* SD threshold, employed to distinguish a pixel as snow/snow-free, was then smoothly increased in small steps (of 0.5 cm). In this manner, by increasing the *in situ* SD threshold, we performed a sensitivity analysis of the satellite-based snow detection with respect to the depth of the snow cover present over the ground.

2) Over Test Site B: We evaluated the performance of the satellite-based snow detection using thresholded FSC information derived from the satellite FSC maps generated using the following approaches:

a) $\mathrm{FSC_{OG:\ TCD}}$ using satellite-derived TCD;
b) $\mathrm{FSC_{OG:\ fVEG}}$ using lidar-derived fVEG;
c) $\mathrm{FSC_{TMSCAG}}$ using endmember-based spectral unmixing.

The normalized confusion matrix elements (as defined in Table II) along with the associated accuracy ($\mathrm{Ac_{obs}}$) and the kappa coefficient (κ) were computed by comparing the snow presence/absence information, obtained from the thresholded satellite FSC maps ($\mathrm{FSC_{TOC}} > 0$), with the thresholded $\mathrm{FSC_{REF}}$ maps. The $\mathrm{FSC_{REF}}$ maps were derived by combining the NCALM (2014) and ASO lidar datasets acquired during the snow depletion phase (March 26, April 17, and May 18, 2016) over Site B.

The metrics were computed from pixels binned at different range of vegetation fraction (fVEG). Each range consisted of

pixels with a 10% increment in the fVEG as compared to the previous range. The pixels were divided (stratified by fVEG) into 10 such ranges indicating an incremental rise in the fVEG.

The performance of the satellite-based FSC retrievals was assessed with respect to the lidar-derived FSC_{REF} using the additional set of statistical evaluation metrics. These were computed both over the incremental range of vegetation fractions (stratified/binned by fVEG) as well as an overall score by considering the entire population of the FSC pixels from all possible range of vegetation fractions together (into a single bin).

V. RESULTS

A. Test Site A: Pyrenees

1) Performance of Satellite-Based Snow Detection: The metrics derived for the satellite-based snow detections over the open (O) and the forested (F) sections (for each plot) are shown in Figs. 3 and 4.

The following observations can be summarized.

1) The sensitivity analysis with respect to the *in situ* SD threshold indicated that the performance (accuracy and κ score) of the algorithm decreased as a function of this threshold. The algorithm performed well even at the lowest SD thresholds that indicated the sensitivity of the algorithm and its ability to capture the finer ground details. Coarse-resolution sensors like MODIS requires the presence of relatively higher levels of SD to corroborate with the groundtruth and achieve similar levels of detection accuracies as high-resolution sensors like Sentinel-2 (and Landsat) [31], [78].

2) Upon comparing Figs. 3 and 4, the metrics from the forested section indicated decrease in the TN and enhancement of the FP. This explained the relatively weaker detection performance over the forested sections as compared to the open areas. The degradation in performance can be cumulatively attributed to the obscuring effect of the canopy cover and consistently lower subcanopy SDs observed over all the plots (Fig. 5), which possibly caused the corresponding decrease in the accuracy and κ score.

3) SD (decreasing order of mean seasonal SD: P4, P2, P1, and P3) solely seems to have little influence in determining the order of the algorithm's performance among the plots. P4 with its North-Eastern aspect exhibited the highest SD, whereas P3 with "Western" aspect had the lowest SD. P2 and P1 with "Eastern" and "Southern" aspect, respectively, exhibited intermediate levels of SD. The performance of the algorithm was rather controlled by a combination of several factors like aspect, canopy cover, "Potential Solar Irradiance" (increasing order of potential irradiance: P4, P2, P3, P1), etc.

4) The highest accuracy and κ score were observed over P1 (upper), as shown in Fig. 3(a). P1 also had the highest level of computed "Potential Solar Irradiance," as detailed in Table I. It is clear from the κ variations that the scores are consistently higher in open areas as compared to the
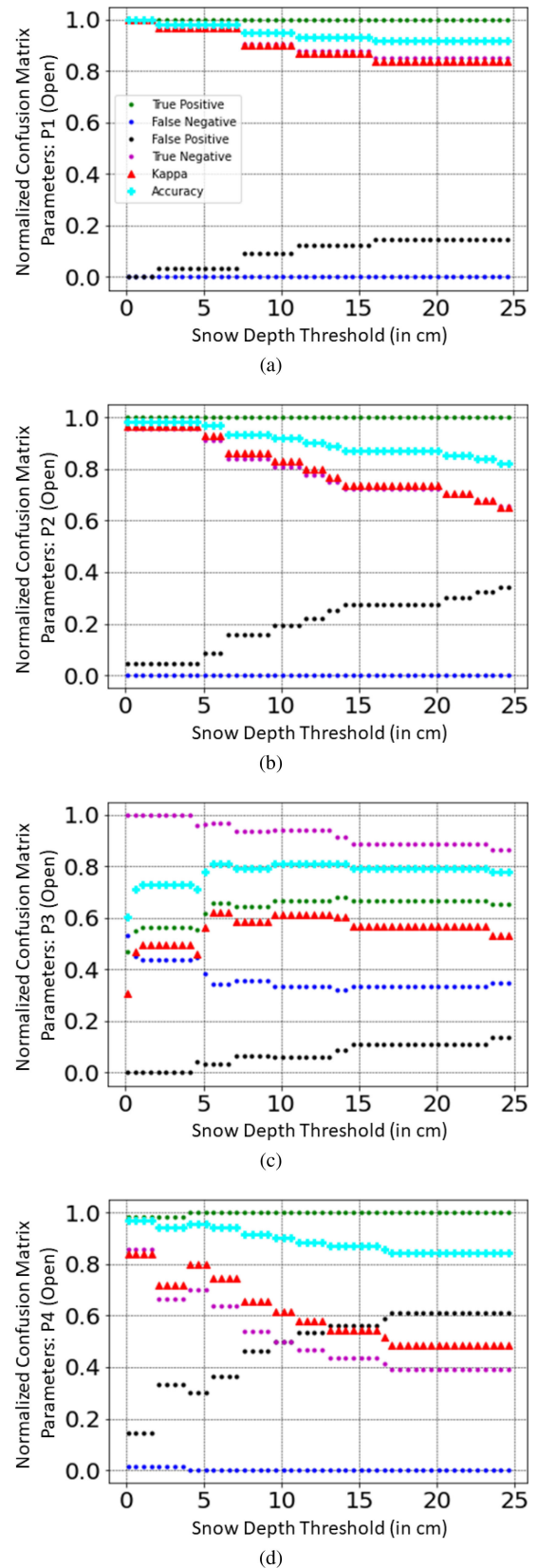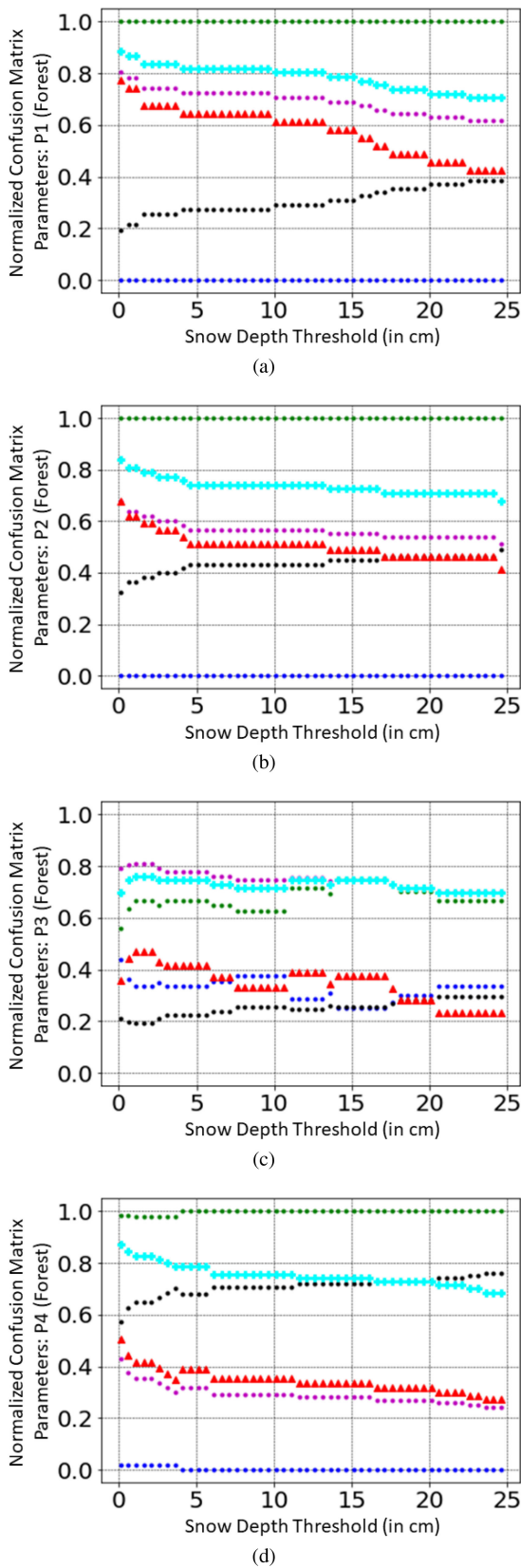

(a)

(b)

(c)

(d)

Fig. 3. Performance assessment of satellite-derived SCA detection over open sections w.r.t. site characteristics and *in situ* snow depth threshold. U: upper and L: lower. Legend: κ: ▲, Ac_{obs}: ✚, TP: ●, TN: ●, FP: ●, and FN: ●.

(a)

(b)

(c)

(d)

Fig. 4. Performance assessment of satellite-derived SCA detection over forest sections w.r.t. site characteristics and *in situ* snow depth threshold. U: upper and L: lower. Legend: ▲, Ac_{obs}: ✚, TP: ●, TN: ●, FP: ●, and FN: ●.
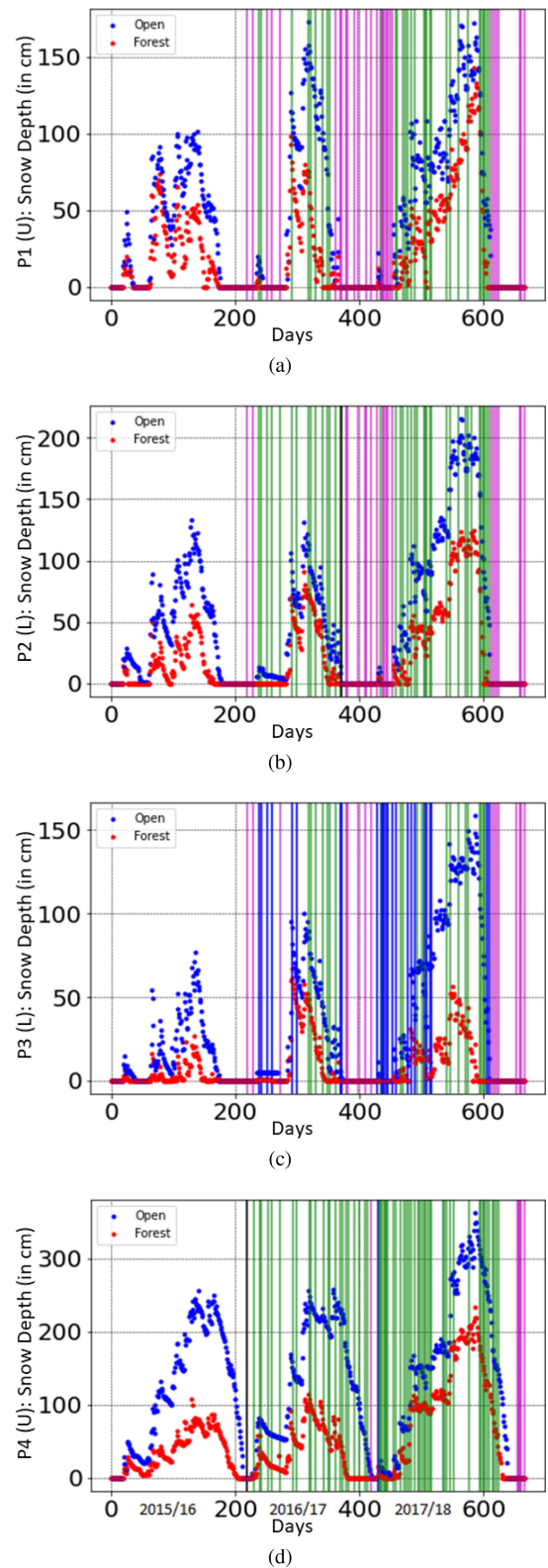

(a)

(b)

(c)

(d)

Fig. 5. Performance of plotwise snow detection w.r.t. *in situ* snow depth (SD) over open (O) section. SD over the open (O) section remains consistently higher than the forest (F) section. Days indicate period of ground data acquisition during the winters of 2015/2016, 2016/2017, and 2017/2018. Legend: TP: ‖‖, TN: ‖‖, FP: ‖‖, FN: ‖‖, and No-Line: Either cloud-covered or absence of S2 data acquisition in 2015/2016.

TABLE III
PLOTWISE SNOW DETECTION METRICS: OPEN (O). TP, TN, FP, AND FN
DENOTE NUMBER OF OCCASION OF SUCCESS/FAILURE OF DETECTION. U:
UPPER AND L: LOWER

Open (O)	P1 (U)	P2 (L)	P3 (L)	P4 (U)
TP	32	40	22	62
TN	29	21	16	6
FP	0	1	0	1
FN	0	0	25	1
Ac_{obs}	1	0.983	0.603	0.971
κ	1	0.964	0.308	0.841

TABLE IV
PLOTWISE SNOW DETECTION METRICS: FOREST (F). TP, TN, FP, AND
FN DENOTE NUMBER OF OCCASION OF SUCCESS/FAILURE OF DETECTION. U:
UPPER AND L: LOWER

Forest (F)	P1 (U)	P2 (L)	P3 (L)	P4 (U)
TP	25	31	14	55
TN	29	21	30	6
FP	7	10	8	8
FN	0	0	11	1
Ac_{obs}	0.885	0.838	0.698	0.871
κ	0.772	0.677	0.356	0.505

forested sections and solar exposure seems to play a prominent role in determining the algorithm's performance.

5) Among all the plots, even though P1 had the highest vegetation density (followed by P3, P2, and P4), it is also the plot with the highest accuracy and κ score. Even though vegetation density is known to be responsible for lowering the performance of satellite-based snow detection, we observed that "Potential Solar Irradiance" had a compensating effect on the performance.

6) The obscuring effect of vegetation cover over P3 (second highest) was not completely compensated by the relatively high "Potential Solar Irradiance" (second highest). This can be attributed to insufficient solar exposure in relation to the canopy cover (to compensate for the obscuring action of the canopy) and low SD (P3 has the lowest SD), which can be cumulatively held responsible for the lowering of the performance (lowest among all).

7) The perturbed nature of the metrics profiles over P3, as shown in Fig. 4(c), can be attributed to the cumulative effect of forest cover and insufficient solar exposure. The former assists in reducing the duration and cumulative snow water equivalent (SWE) of the snowpack (due to reduced SD) along with introducing manifold increase in the spatial heterogeneity (by 190% [37]) of the subcanopy snow cover. Whereas the latter constraints the compensating action under the canopy cover and thus limits the essential spectral information (reflected from the snow covered forest floor) from reaching the satellite sensor.

We investigated the role of these site factors in the success/failure of the algorithm (in correctly identifying a snow covered pixel) in the presence of a finite SD (considering the SDs in the open section). The plotwise performance can be visually appreciated in Fig. 5 (with the confusion matrix elements plotted as colored lines).

The overall accuracy and κ score (for the entire SD time-series) for the minimum SD threshold (for all SD > 0.1 cm) are detailed in Tables III and IV (considering the SDs in the open and forested sections, respectively).

The following can be summarized from these observations.

1) The algorithm's performance (decreasing order of performance: P1, P2, P4, and P3) correlated better with the "Potential Solar Irradiance" as compared to the "Observed Solar Irradiance," as detailed in Table I. Due to the point-based measurement of the observed irradiance in the forest openings, which is also impacted by the sheltering effect of the surrounding trees, a difference can be recognized

between the potential and observed irradiance. Moreover, a satellite pixel is spatially heterogeneous and can accommodate both the forest opening and the adjoining trees within a single pixel. This can hamper the user's ability to distinctly correlate an algorithm's performance with one of the irradiances.

2) Furthermore, the satellite acquired surface reflectance is dependent on the state and geometry of solar illumination (a seasonally changing factor over the site) during the time of the satellite scene acquisition, which is responsible for illuminating the subcanopy snow cover. Under forested conditions, a significant portion of the incoming as well as the reflected light from the snow covered forest floor is absorbed by the overlying vegetation (for photosynthesis) that can consequently reduce the reflectance from the forest floor. This process can eventually hamper the satellite detection of subcanopy snow cover. Terrain shadowing can also limit detection.

3) It is noteworthy that over the open section (Table III) both FP (Error of Commission) and FN (Error of Omission) are negligibly small with the only exception of P3 where FN is noticeably high. The introduction of FP is evident only in the forested section (Table IV) with the FN still remaining quite small and the only exception can be observed again over P3. The poor performance of the algorithm over P3 (lowest) can be visually observed in Fig. 5(c) by the abundance of FN (blue lines) that indicates cases when a snow covered pixel was misclassified as snow-free by the satellite algorithm. Over both the sections, under well-illuminated conditions (except P3), the FN (Error of Omission) remained significantly low indicating that the thinnest layer of snow (in situ data) was detected.

4) The role of site factors associated with P3 is reflected in the way they influence the metrics in a deteriorating manner. Low κ indicates the algorithm's inability to corroborate with the in situ observations and identification of snow pixels. Even a sufficiently high value of "Potential Solar Irradiance" (second highest), as detailed in Table I, was unable to compensate due to the unique site characteristics: shadowed conditions due to low elevation at the bottom of the valley as shown in Fig. 1(c), relatively high canopy cover (second highest), and low SD (lowest).

5) The accuracy and κ score over all the plots (except P3) showed better performance with respect to the SD measured over the open areas. Over P3 (in Table III with respect to Table IV), TP increased, TN decreased, FP

decreased, and FN increased. This cumulatively led to a counterintuitively small decrease in the performance metrics (since increase in FN was greater than increase in TP) for the open areas as compared to the forested section.

B. Test Site B: Sierra Nevada

1) Performance of Satellite-Based Snow Detection: The lidar-derived FSC_{REF} map on March 26, 2016 is as shown in Fig. 6(a).

The performance of the satellite-based snow detection was assessed using the normalized confusion matrix elements as shown in Fig. 7, derived by comparing the thresholded lidar-derived maps with the binarized satellite-derived FSC (for the SCA analysis, the thresholded/binarized FSC maps are also referred to as $FSC_{OG: TCD}$, $FSC_{OG: fVEG}$, and FSC_{TMSCAG}) that employed S2 acquisition on the same date and the L7 acquisition on March 24 (for FSC_{TMSCAG}).

The following observations can be summarized from Fig. 7.
1) The accuracy and the κ coefficient decreased for increasing values of fVEG. This can be attributed to the decrease in the TP and increase in the FN due to the growing degree of obscuration by the overlying canopy cover.
2) The metric profiles of the $FSC_{OG: TCD}$ and $FSC_{OG: fVEG}$ showed little difference. This indicated that the Landsat reflectance derived TCD (at a coarser resolution) captured the ground vegetation fraction information reliably close to the lidar-derived fVEG, which was acquired at a comparatively higher resolution (1 m) and then aggregated (1 m pixels comprised a 10 m fVEG pixel) before it was resampled to 20 m (or 30 m for L7/8 on other dates).
3) Although Fig. 7(b) indicated similar levels of accuracy as Fig. 7(a), the κ coefficient revealed the disagreement between the snow cover information obtained from the FSC_{TMSCAG} (L7 on March 24) and the ground conditions (ASO on March 26). This disagreement can possibly be attributed to a light snow precipitation event (or wind-transport of snow) that occurred over Site B between March 24 and March 26, 2016 before the Sentinel-2 and lidar data acquisitions. This event was evident in the meteorological reanalyses and was recorded during this period at the Lake Independence SNOTEL station (2 mm of precipitation is recorded between March 25 and March 26 at station # 541).

The FSC_{REF} map over Site B on April 17, as shown in Fig. 8(a), indicates the ablating effect of rising air temperature (refer to [38, Fig. 1(D)]) on the snow cover extent over the area, particularly in the lower elevations (refer to [38, Fig. 2]). L8 overlapped the lidar acquisition on this date.

The confusion matrix metrics are as shown in Fig. 9.

The following observations can be summarized.
1) An increase in the TN and a decrease in the FP can be observed in Fig. 9 with respect to the profile in Fig. 7. This enhancement in the "True" and reduction in the "False" element of the confusion matrix can be attributed to the decrease in the FSC_{TOC} due to depleting trend of the snow cover. For a given value of vegetation density, FSC_{TOC}
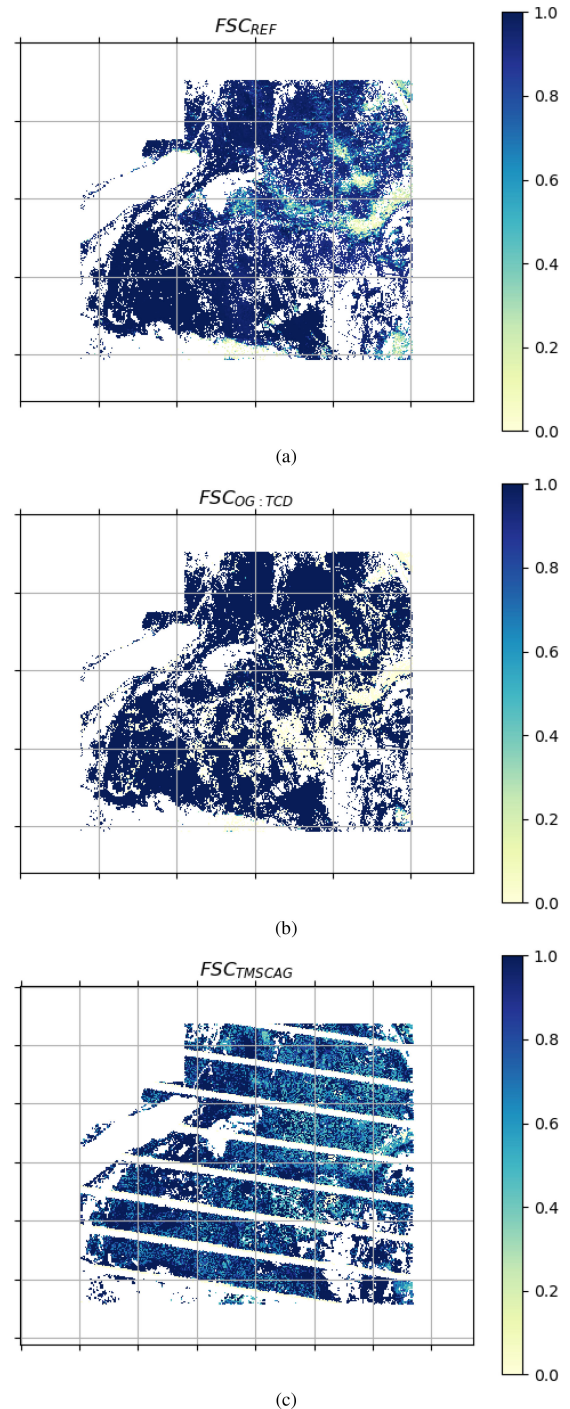

Fig. 6. FSC_{REF} (ASO + NCALM), $FSC_{OG: TCD}$ (S2), and FSC_{TMSCAG} (L7) maps over Site B: March 2016. Satellite: S2 on March 26 and L7 on March 24, 2016. Lidar: ASO on March 26, 2016 and NCALM in 2014.

beyond a critical value can cause overestimation while canopy adjusting it to FSC_{OG} due to the saturation of the scaling function [44]. Such a saturating action can cause overestimated subcanopy snow cover information, which can be eventually falsely classified (increasing the FP) as a snow covered pixel. Therefore, a decrease in the FP is an indication of decrease in such overestimations.
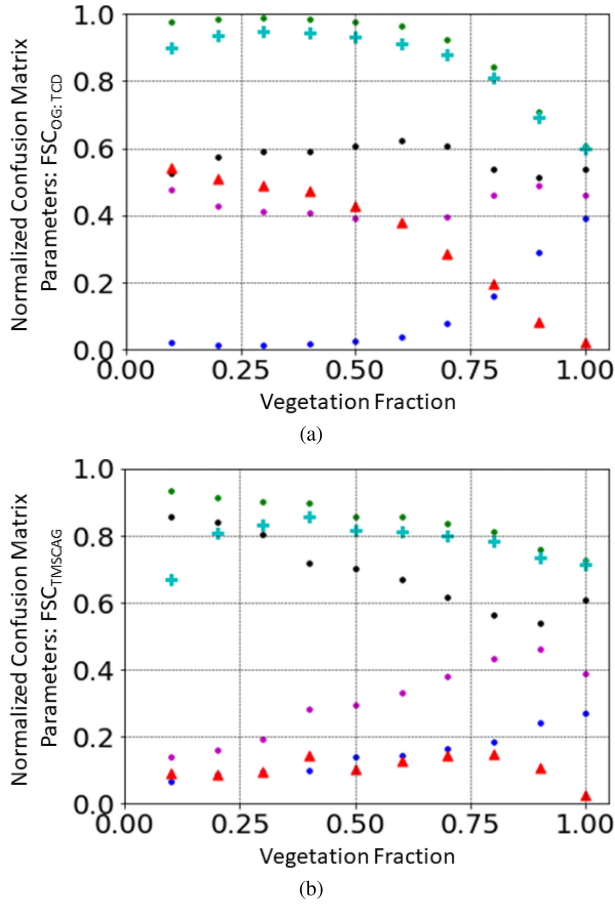
Fig. 7. Performance assessment of satellite-derived SCA w.r.t. vegetation fraction: March 2016. Satellite: S2 on March 26 and L7 on March 24, 2016. Lidar: ASO on March 26, 2016 and NCALM in 2014. Legend: κ: ▲, Ac_{obs}: ✚, TP: ●, TN: ●, FP: ●, and FN: ●.

Fig. 8. FSC_{REF} (ASO + NCALM), $FSC_{OG:\ TCD}$ (L8), and FSC_{TMSCAG} (L8) maps over Site B: April 2016. Satellite: L8 on April 17, 2016. Lidar: ASO on April 17, 2016 and NCALM in 2014.

2) As the snow cover depleted, the steepness of the decrease in the TP and increase in the FN (with increasing canopy density) decreased. This indicated a decrease in the negative correlation between the algorithm's performance and vegetation density due to the earlier disappearance of the subcanopy snow cover. However, in case of the FSC_{TMSCAG}, it indicated a relatively sharper fall in the TP and a steeper rise in the FN, both commencing at a relatively lower value of vegetation fraction (commencing from fVEG > 0.25). This indicated the inability of the FSC_{TMSCAG} to appropriately identify subcanopy SCAs (increasing FN).

3) An initial rise in both the accuracy and κ coefficient was observed with increasing vegetation fraction range, which however later decreased. This indicated that the introduction of TCD or fVEG information to FSC_{TOC} indeed improved the subcanopy FSC (FSC_{OG}) until a critical value of the vegetation density was reached beyond which the metrics decreased.

4) Unlike the FSC_{TMSCAG} metrics in Fig. 7(b), Fig. 9(b) showed a higher degree of resemblance to the metrics generated for $FSC_{OG:\ TCD}$ and $FSC_{OG:\ fVEG}$, which can be attributed to any lack of temporal gap or a decorrelating
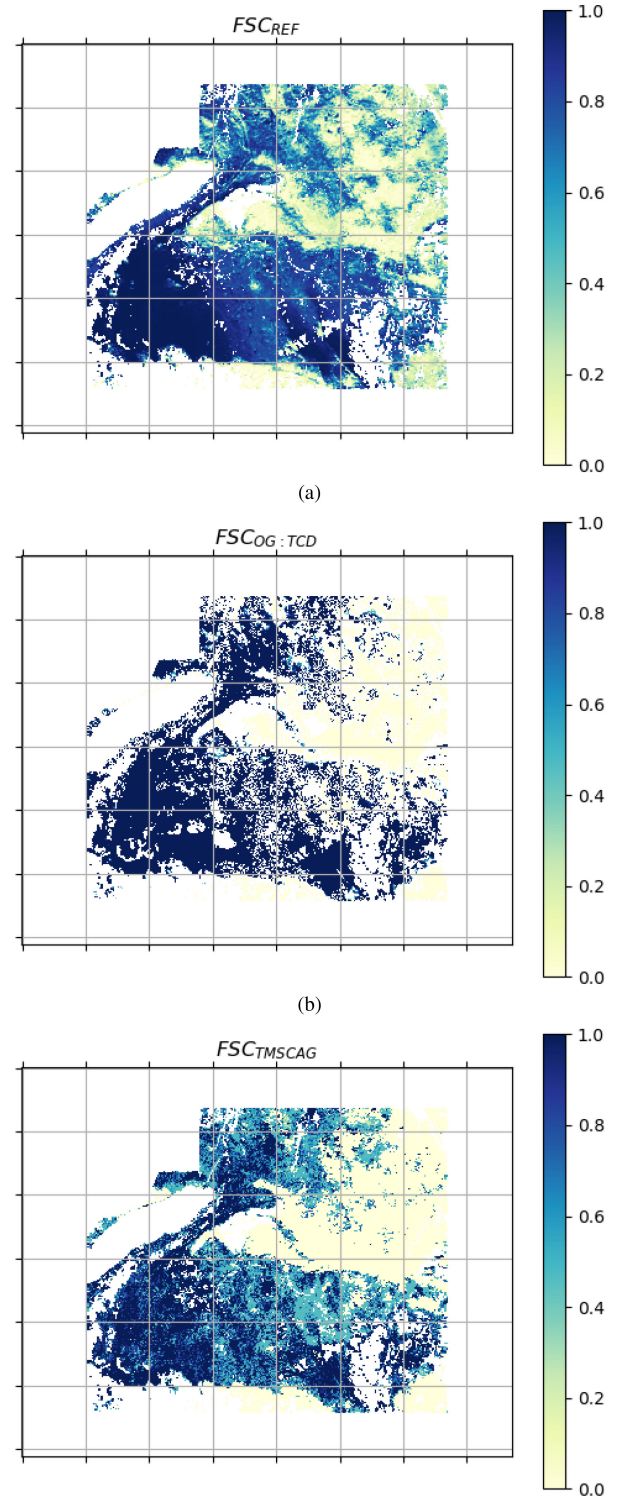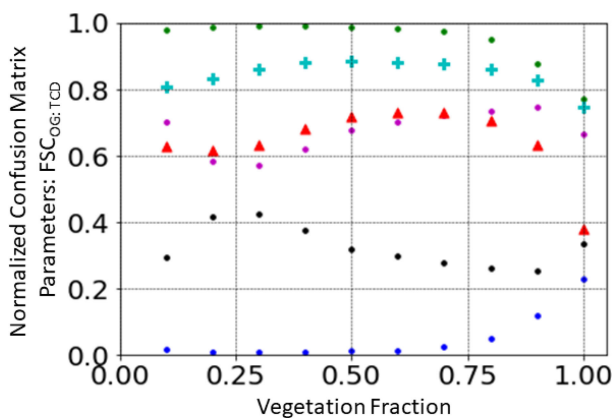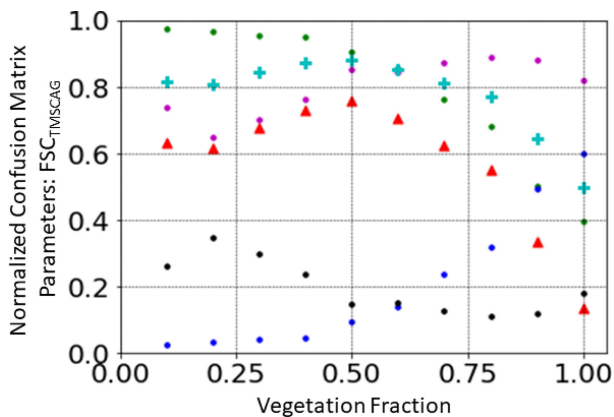
precipitation (or wind-transport) event between the satellite and lidar acquisitions.

5) A relatively higher value of κ coefficient as compared to Fig. 7 indicated a better agreement of the satellite-derived FSC with the lidar-based measurements.
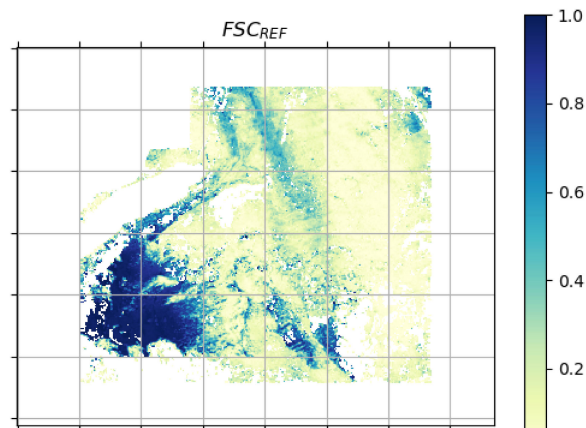
(a)

(b)

Fig. 9. Performance assessment of satellite-derived SCA w.r.t. vegetation fraction: April 2016. Satellite: L8 on April 17, 2016. Lidar: ASO on April 17, 2016 and NCALM in 2014. Legend: κ: ▲, Ac_{obs}: ✚, TP: ●, TN: ●, FP: ●, and FN: ●.

(a)

(b)

(c)

Fig. 10. FSC$_{\text{REF}}$ (ASO + NCALM), FSC$_{\text{OG: TCD}}$ (L7), and FSC$_{\text{TMSCAG}}$ (L7) maps over Site B: May 2016. Satellite: L7 on May 27, 2016. Lidar: ASO on May 18, 2016 and NCALM in 2014.
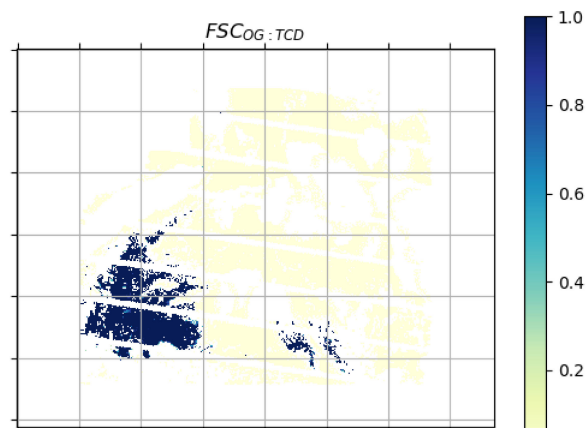
The FSC$_{\text{REF}}$ over Site B on May 18, 2016 can be observed in Fig. 10(a). A visual inspection of the snow cover extent with respect to elevation profile and vegetation fraction (refer to [38, Fig. 2]) indicated that the vast majority of the remnant snow cover was limited to the south-west corner of the site that offered a suitable combination of high elevation (highest in the area) and low vegetation density (low fVEG).

The closest cloud-free satellite scene to compare the ground scenario was a L7 scene available on May 27, 2016. The following observations can be summarized from the confusion matrix metrics shown in Fig. 11.
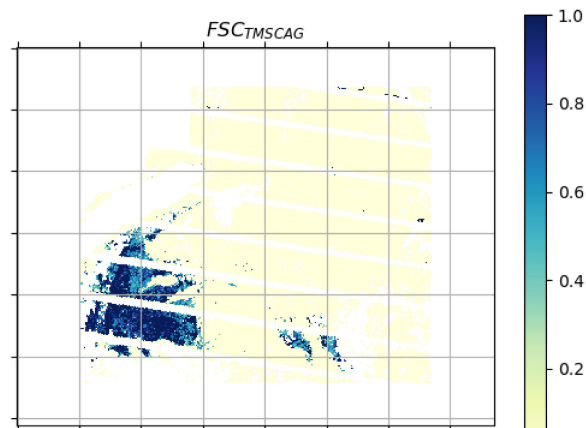
1) FP gradually decreased with the depleting trend of snow cover from March to May 2016. TP and TN are maximized, whereas FP and FN are minimized.

2) Although the accuracy profile remained relatively flat, the κ coefficient improved with initial increase in the vegetation fraction and later showed a decrease. The general rise in the κ score can be attributed to overall improvement in the identification of snow cover under nonsaturating conditions when FSC$_{\text{TOC}}$ is accurately rescaled to FSC$_{\text{OG}}$. For certain combinations of top-of-the-canopy snow cover and vegetation fraction (VGF or TCD), (3) can saturate resulting in overestimation.

3) Although the majority of snow cover was only limited to the high elevation and sparsely vegetated south-west corner of the test site, the decrease in κ for higher ranges of vegetation fraction with increasing FN indicated the
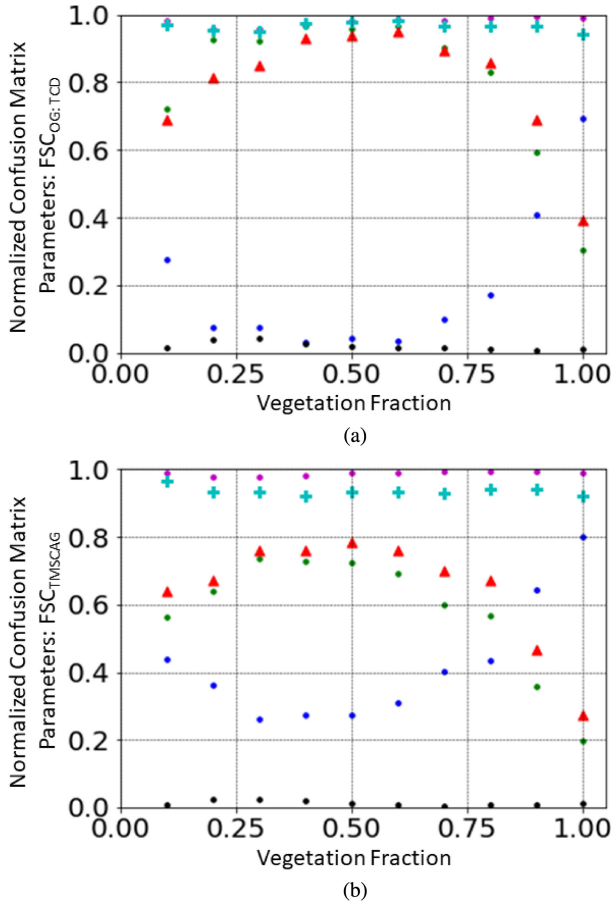
Fig. 11. Performance assessment of satellite-derived SCA w.r.t. vegetation fraction: May 2016. Satellite: L7 on May 27, 2016. Lidar: ASO on May 18, 2016 and NCALM in 2014. Legend: κ: ▲, Ac_{obs}: ✚, TP: ●, TN: ●, FP: ●, and FN: ●.

Fig. 12. Violin plots indicating depleting trend of the FSC over Site B from March to May 2016. (a) March 2016. (b) April 2016. (c) May 2016.

algorithm's missed detection of some sparse remnant snow cover still present under the dense vegetation.

4) As the majority of subcanopy snow cover disappeared between March 26 and May 27, the κ score improved. This indicated that the satellite detection of terrestrial snow cover more accurately resembles the actual ground scenario when the snow cover is limited to the open or sparsely vegetated areas rather than under the dense forest cover.

5) For snow cover information obtained from the FSC_{TMSCAG}, both TP and κ remained comparatively lower and FN relatively higher.

The depleting state of snow cover over Site B as indicated in Figs. 6, 8, and 10 can be appreciated in the violin plots as shown in Fig. 12. These plots indicate the shifting regime of snow cover (from high toward low FSC) over the snow depletion phase of the winter of 2016 over Site B. The distribution of the FSC on March 26 was prominently dominated by high FSC near 80%–100% [Fig. 12(a)]. As snow cover depleted over Site B, the pixel FSC distribution gradually developed a spread along the length of the "violins" as can be observed through the bulging-up of the central section in Fig. 12(b) on April 17. As the majority of the snow cover depleted over the area, the pixel distribution
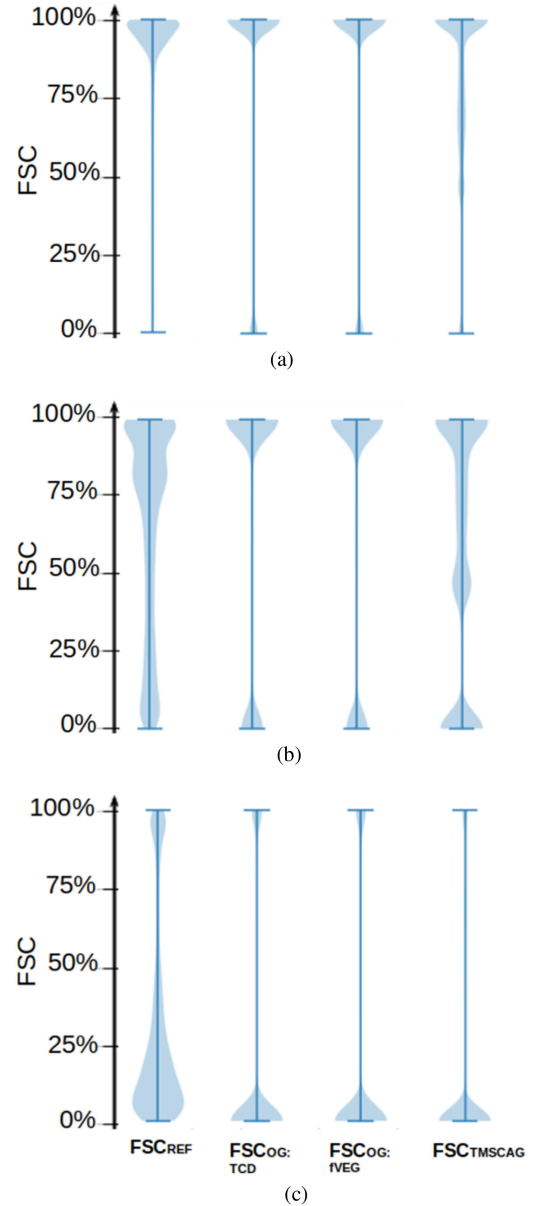
prominently shifted towards lower FSCs near the bottom of the "violins" [Fig. 12(c)].

2) Performance of Satellite-Based FSC: The RMSE and CC metrics computed for satellite-based FSC estimated on March 26, 2016 (unlike the SCA analysis, the FSC maps are not thresholded/binarized into snow/no-snow for the FSC analysis) are shown in Fig. 13(a) and (b). The following observations can be summarized.

1) A general trend among the metrics can be observed here. As the vegetation fraction increased, the RMSE initially decreased due to the correcting effect of the FSC_{TOC}-FSC_{OG} scaling function. This function, beyond a critical combination of FSC_{TOC} and vegetation fraction, overestimated the FSC_{OG}, which then caused an increase in the
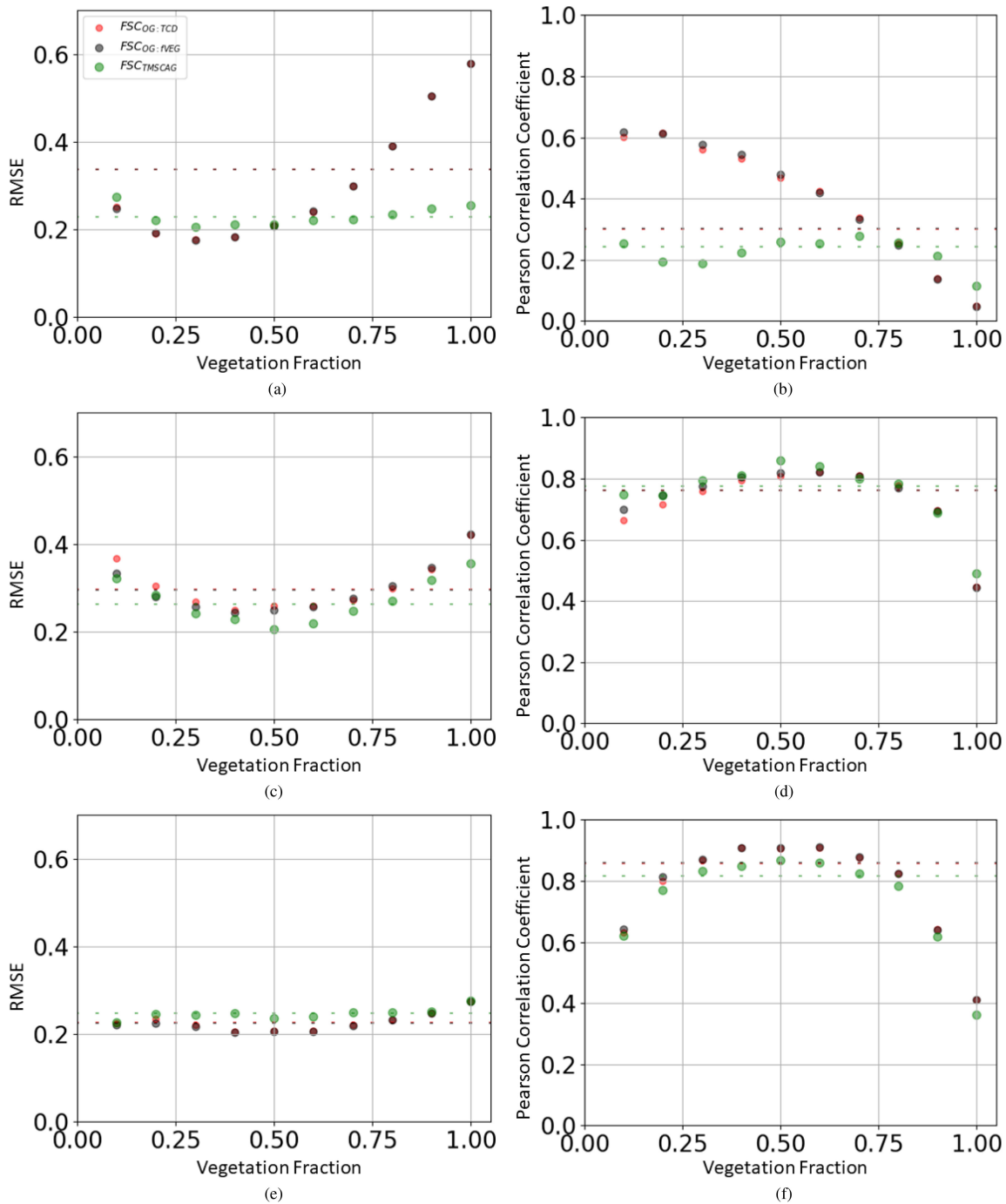
Fig. 13. Performance assessment of satellite-derived FSC w.r.t. temporal dynamics of snow cover and vegetation fraction. As snow cover over Site B depletes from March to May, both the vegetation fraction binned RMSE and the overall RMSE decreases and the vegetation fraction binned CC and the overall CC increases. (a) RMSE: March 2016. (b) CC: March 2016. (c) RMSE: April 2016. (d) CC: April 2016. (e) RMSE: May 2016. (f) CC: May 2016. Dashed lines indicate overall metrics for the entire image by considering FSCs from all vegetation fractions together. RMSE: Root mean square error and CC: Pearson correlation coefficient.

RMSE. Pearson CC decreased with increasing vegetation cover and the decrease was steeper at higher vegetation fractions.

2) Due to the decorrelating precipitation event that occurred between the L7 and the lidar data acquisitions, significant separation can be observed for the FSC_{TMSCAG} at certain vegetation ranges among the computed metrics. The FSC_{TMSCAG}, generated using the L7 acquisition on March

24, indicated a low RMSE at higher vegetation fraction range. This can be attributed possibly to the overestimation that occurred with the S2 derived FSC_{OG} due to relatively larger FSC_{TOC}, as a result of the precipitation.

3) It is difficult to assign the source of error while considering the overall global score (dashed lines) since it can be realized from Fig. 13 that error is rather unevenly distributed

TABLE V
OVERALL STATISTICS FOR SATELLITE-DERIVED FSC OVER SITE B. BY
CONSIDERING FSCs AT ALL VEGETATION FRACTIONS TOGETHER

	$FSC_{OG: TCD}$	$FSC_{OG: fVEG}$	FSC_{TMSCAG}
March 2016			
RMSE	0.336	0.337	0.297
CC	0.301	0.301	0.153
April 2016			
RMSE	0.296	0.296	0.263
CC	0.761	0.762	0.776
May 2016			
RMSE	0.226	0.225	0.247
CC	0.857	0.859	0.814

across the different range of vegetation fractions. Therefore, the performance assessment of the FSC algorithm is more apparent when the metrics are computed for each individual range of fVEG.

The metrics computed on April 17 are shown in Fig. 13(c) and (d). The following observations can be summarized.

1) The metric profiles indicated the same trend as Fig. 13(a) and (b) but are relatively flatter. This can be attributed to the disappearing top-of-the-canopy snow cover that allows accurate rescaling and determination of the FSC_{OG} closely matching the actual ground conditions. The flatness of the metrics curve can be contributed partly due to the slightly coarser resolution of the L8 data (30 m as compared to 20 m for S2).

2) Unlike the disparity of the FSC_{TMSCAG} with the ground conditions as observed in Fig. 13(a) and (b) due to the absence of temporally decorrelating precipitation/wind-transport event on April 17, all metrics for this date followed a nearly coherent path.

The next lidar data collection over Site B occurred on May 18, 2016. However, the closest cloud-free scene (L7) was only possible on May 27. The metrics for this acquisition are shown in Fig. 13(e) and (f). The following observations can be summarized.

1) The RMSE demonstrated an even flatter profile as compared to the ones observed in Fig. 13(a) and (c). This denoted an almost negligible variation in the RMSE with respect to the vegetation fraction for scenarios where the majority of snow cover was limited to sparsely vegetated and open areas.

2) The CC increased and remained fairly unchanged until it showed a decrease again for densely vegetated areas (fVEG > 0.75).

In summary, a closer inspection of Fig. 13 indicated that the overall global RMSE decreased and the Pearson CC increased (both denoted by the dashed lines) from March 26 to May 27, 2016. The overall variation in the statistics during this period is summarized in Table V. The improving performance of the algorithm with respect to the ablating state of snow cover over Site B can be observed both from the variation in the vegetation fraction binned and overall statistics. It can be observed that the $FSC_{OG: TCD}$ and $FSC_{OG: fVEG}$ demonstrated better or similar overall performance with regard to FSC_{TMSCAG}.

VI. DISCUSSION

This assessment indicated that accurate detection of binary snow cover (SCA) was achieved with the NDSI-based operational MAJA-LIS algorithm in forested areas despite the obstructing effect of the canopy cover. Since TCD plays an additional role in the estimation of the under canopy FSC, its performance was separately evaluated. The presence/absence of snow cover (binary SCA) conveys little information regarding the performance of the FSC estimation (snow cover fraction is a continuously varying quantity from 0 to 1), particularly under varying degree of vegetation fraction conditions. The accuracy generally exceeded 0.9 and a κ of about 0.6 was obtained in areas with low to average TCD over both the test sites. However, analyses over the Sierra Nevada site indicated that the performance of the SCA algorithm dropped in areas with high TCDs (typically TCD > 0.75), and the snow detection was not significantly better than a random agreement at TCD=1. Over the Pyrenees site, the largest decrease in performance was observed in shaded forested slopes, where both canopy cover and the lack of solar irradiance collectively created the most challenging observation scenario. This is well in accordance with observations reported by early investigations where snowpack obscured by shadow or forest cover hampered the photointerpretation of snowlines in watersheds and recent investigations that reported areas of dense forest shadows to be primarily responsible for introducing omission/commission errors in snow detection algorithms [79], [80].

Aspects facing away from the solar illumination, increasing canopy cover and decreasing exposure to solar irradiance, negatively impacted the performance of the snow detection. Nevertheless, the solar irradiance compensated for the obscuring action of the dense canopy cover over a south facing test plot (P1). Under well-illuminated conditions, the FN remained significantly low (mostly zero) that indicated there was negligible omission errors both in the open and under the canopy in the over the Pyrenees site (except P3).

In general, the accuracy of the FSC algorithm decreased with an increase in the vegetation fraction and remained relatively lower than those observed over the open areas (25% as reported in [32]). This observed trend in the accuracy, graphically illustrated in this investigation, corroborates well with lower accuracies reported by past investigations with snow detection and fSCA estimation over forested areas and complex terrains [25],[81]–[85]. The investigation indicated close resemblance of the LIS FSC_{OG} rescaled using both high-resolution lidar-derived and coarse-resolution satellite-derived fractional vegetation maps (fVEG and TCD, respectively). This revealed that using a more accurate TCD product may not lead to significant improvements in the FSC retrievals. Therefore, it can be inferred that apart from the different methodologies followed by the algorithms, the performance was largely limited by the radiometric information content of the satellite scenes. The reliability of both the operational and TMSCAG-based FSC retrievals was observed to be limited beyond a critical value of TCD (typically, TCD > 0.75). Despite very different approaches, FSC_{OG} and FSC_{TMSCAG} indicated similar performances and FSC_{TMSCAG} performed only slightly better under certain site

conditions. However, the current registration performances of S2 L1C products are not nominal and the upcoming reprocessing by the European Space Agency (ESA) may lead to improved performances in many S2 products including FSC.

VII. Conclusion

We investigated the performance of NDSI-based SCA and FSC algorithms with high-resolution Sentinel-2 and Landsat-7/8 data in two forested landscapes (Pyrenees and Sierra Nevada). These algorithms are employed by the recently launched operational HR-S&I monitoring service. Over the Pyrenees site, the operational snow cover detection algorithm exhibited better performance in areas receiving higher solar irradiance, but the detection degraded under dense canopy and poorly illuminated forest conditions. Over the Sierra Nevada site, the HR-S&I snow cover fraction retrievals were comparable (25%–30% RMSE) to those provided by the USGS, based on a spectral unmixing approach. However, uncertainties with the snow cover fraction retrieved over dense forested areas remained large, and the retrievals were not considered reliable in areas with tree cover densities above 75%. Over the Sierra Nevada, we employed the lidar-derived vegetation fraction map (fVEG) along with the default the Landsat time-series data derived tree cover density (TCD) map. One of the key observations from this experiment revealed that the use of a more accurate high-resolution fVEG map derived from airborne lidar did not improve the subcanopy FSC retrievals. Hence, we suspect that the accuracy is rather limited by the algorithm and the physical limits due to the masking of the subcanopy snow cover by the overlying trees, which obstructs the useful signal from reaching the satellite sensors. Therefore, the quality of the vegetation density data is not solely responsible for determining the performance of the retrievals. Nevertheless, it remains to be investigated if seasonally variable TCD information could possibly help in improving such retrievals, especially over the deciduous forests.

References

[1] R. L. Armstrong and E. Brun, *Snow and Climate: Physical Processes, Surface Energy Exchange and Modeling.* Cambridge, U.K.: Cambridge Univ. Press, 2008.

[2] J. C. Barnes and C. J. Bowley, "Snow cover distribution as mapped from satellite photography," *Water Resour. Res.*, vol. 4, no. 2, pp. 257–272, 1968.

[3] A. J. Dietz, C. Kuenzer, U. Gessner, and S. Dech, "Remote sensing of snow-a review of available methods," *Int. J. Remote Sens.*, vol. 33, no. 13, pp. 4094–4134, 2012.

[4] C. Dong and L. Menzel, "Snow process monitoring in montane forests with time-lapse photography," *Hydrol. Processes*, vol. 31, no. 16, pp. 2872–2886, 2017.

[5] E. H. Czyzowska-Wisniewski, W. J. van Leeuwen, K. K. Hirschboeck, S. E. Marsh, and W. T. Wisniewski, "Fractional snow cover estimation in complex alpine-forested environments using an artificial neural network," *Remote Sens. Environ.*, vol. 156, pp. 403–417, 2015.

[6] K. E. Bennett, J. E. Cherry, B. Balk, and S. Lindsey, "Using modis estimates of fractional snow cover area to improve streamflow forecasts in interior alaska," *Hydrol. Earth Syst. Sci.*, vol. 23, no. 5, pp. 2439–2459, 2019.

[7] J. Foster, "The significance of the date of snow disappearance on the arctic tundra as a possible indicator of climate change," *Arctic Alpine Res.*, vol. 21, no. 1, pp. 60–70, 1989.

[8] I. IPCC Contribution of Working Groups I, R. P. III (Core Writing Team, and L. M., Eds.), "Fifth assessment report of the intergovernmental panel on climate change," Accessed: Feb. 1, 2021. 2014. [Online]. Available: https://archive.ipcc.ch/report/ar5/syr/

[9] E. Malnes *et al.*, "User requirements for the snow and land ice services-cryoland," *Cryosphere*, vol. 9, no. 3, pp. 1191–1202, 2015.

[10] S. G. Warren, "Optical properties of snow," *Rev. Geophys.*, vol. 20, no. 1, pp. 67–89, 1982.

[11] D. K. Hall, G. A. Riggs, and V. V. Salomonson, "Development of methods for mapping global snow cover using moderate resolution imaging spectroradiometer data," *Remote Sens. Environ.*, vol. 54, no. 2, pp. 127–140, 1995.

[12] F. R. Valovcin, "Snow/cloud discrimination," AFGL-TR-76-0174, Air Force Surveys in Geophysics, No. 349, Meteorology Division Project 6698, Air Force Geophysics Laboratory, Air Force Systems Command, UASF.

[13] J. Dozier, "Spectral signature of alpine snow cover from the landsat thematic mapper," *Remote Sens. Environ.*, vol. 28, no. 1, pp. 9–22, 1989.

[14] Q. Zhang, T. Yao, K. F. Huemmrich, E. M. Middleton, A. Lyapustin, and Y. Wang, "Evaluating impacts of snow, surface water, soil and vegetation on empirical vegetation and snow indices for the utqiaġvik tundra ecosystem in alaska with the lvs3 model," *Remote Sens. Environ.*, vol. 240, 2020, Art. no. 111677.

[15] S. Metsämäki, J. Vepsäläinen, J. Pulliainen, and Y. Sucksdorff, "Improved linear interpolation method for the estimation of snow-covered area from optical data," *Remote Sens. Environ.*, vol. 82, no. 1, pp. 64–78, 2002.

[16] Q. Xin, C. E. Woodcock, J. Liu, B. Tan, R. A. Melloh, and R. E. Davis, "View angle effects on modis snow mapping in forests," *Remote Sens. Environ.*, vol. 118, pp. 50–59, 2012.

[17] J. M. Chen and J. Cihlar, "Retrieving leaf area index of boreal conifer forests using landsat TM images," *Remote Sens. Environ.*, vol. 55, no. 2, pp. 153–162, 1996.

[18] J. Liu, R. A. Melloh, C. E. Woodcock, R. E. Davis, and E. S. Ochs, "The effect of viewing geometry and topography on viewable gap fractions through forest canopies," *Hydrol. Processes*, vol. 18, no. 18, pp. 3595–3607, 2004.

[19] T. Nilson and U. Peterson, "Age dependence of forest reflectance: Analysis of main driving factors," *Remote Sens. Environ.*, vol. 48, no. 3, pp. 319–331, 1994.

[20] T. H. Painter, K. Rittger, C. McKenzie, P. Slaughter, R. E. Davis, and J. Dozier, "Retrieval of subpixel snow covered area, grain size, and albedo from modis," *Remote Sens. Environ.*, vol. 113, no. 4, pp. 868–879, 2009.

[21] E. H. Bair, T. Stillinger, and J. Dozier, "Snow property inversion from remote sensing (spires): A generalized multispectral unmixing approach with examples from modis and landsat 8 oli," *IEEE Trans. Geosci. Remote Sens.*, early access, Dec. 10, 2020, doi: 10.1109/TGRS.2020.3040328.

[22] T. Masson *et al.*, "An assessment of existing methodologies to retrieve snow cover fraction from modis data," *Remote Sens.*, vol. 10, no. 4, 2018, Art. no. 619.

[23] K. Aalstad, S. Westermann, and L. Bertino, "Evaluating satellite retrieved fractional snow-covered area at a high-arctic site using terrestrial photography," *Remote Sens. Environ.*, vol. 239, 2020, Art. no. 111618.

[24] D. K. Hall, G. A. Riggs, V. V. Salomonson, N. E. DiGirolamo, and K. J. Bayr, "Modis snow-cover products," *Remote Sens. Environ.*, vol. 83, no. 1-2, pp. 181–194, 2002.

[25] M. S. Raleigh, K. Rittger, C. E. Moore, B. Henn, J. A. Lutz, and J. D. Lundquist, "Ground-based testing of modis fractional snow cover in subalpine meadows and forests of the sierra nevada," *Remote Sens. Environ.*, vol. 128, pp. 44–57, 2013.

[26] J. Dozier, E. H. Bair, and R. E. Davis, "Estimating the spatial distribution of snow water equivalent in the world's mountains," *Wiley Interdiscipl. Rev.: Water*, vol. 3, no. 3, pp. 461–474, 2016.

[27] N. C. Cristea, I. Breckheimer, M. S. Raleigh, J. HilleRisLambers, and J. D. Lundquist, "An evaluation of terrain-based downscaling of fractional snow covered area data sets based on lidar-derived snow data and orthoimagery," *Water Resour. Res.*, vol. 53, no. 8, pp. 6802–6820, 2017.

[28] E. E. Berman, D. K. Bolton, N. C. Coops, Z. K. Mityok, G. B. Stenhouse, and R. D. Moore, "Daily estimates of landsat fractional snow cover driven by modis and dynamic time-warping," *Remote Sens. Environ.*, vol. 216, pp. 635–646, 2018.

[29] K. Rittger, M. S. Raleigh, J. Dozier, A. F. Hill, J. A. Lutz, and T. H. Painter, "Canopy adjustment and improved cloud detection for remotely sensed snow cover mapping," *Water Resour. Res.*, vol. 56, no. 6, 2020, Art. no. e 2019WR024914.

[30] E. E. Agency, "Pan-european high-resolution snow & ice monitoring of the copernicus land monitoring service: Production of basic products, ATBD," Accessed: Feb. 1, 2021. 2020. [*Online*]. Available: https://land.copernicus.eu/user-corner/technical-library/hrsi-snow-atbd

[31] S. Gascoin, M. Grizonnet, M. Bouchet, G. Salgues, and O. Hagolle, "Theia snow collection: High-resolution operational snow cover maps from sentinel-2 and landsat-8 data," *Earth Syst. Sci. Data*, vol. 11, no. 2, pp. 493–514, 2019.

[32] S. Gascoin *et al.*, "Estimating fractional snow cover in open terrain from sentinel-2 using the normalized difference snow index," *Remote Sens.*, vol. 12, no. 18, 2020, Art. no. 2904.

[33] M. W. Baba, S. Gascoin, and L. Hanich, "Assimilation of sentinel-2 data into a snowpack model in the high atlas of morocco," *Remote Sens.*, vol. 10, no. 12, p. 23, 2018. [Online]. Available: https://www.mdpi.com/2072-4292/10/12/1982

[34] D. J. Selkowitz, R. R. Forster, and M. K. Caldwell, "Prevalence of pure versus mixed snow cover pixels across spatial resolutions in alpine environments," *Remote Sens.*, vol. 6, no. 12, pp. 12 478–12508, 2014.

[35] I. Appel, "Uncertainty in satellite remote sensing of snow fraction for water resources management," *Front. Earth Sci.*, vol. 12, no. 4, pp. 711–727, 2018.

[36] L. Matikainen, R. Kuittinen, and J. Vepsäläinen, "Estimating drainage area-based snow-cover percentages from NOAA AVHRR images," *Int. J. Remote Sens.*, vol. 23, no. 15, pp. 2971–2988, 2002.

[37] A. Sanmiguel-Vallelado *et al.*, "Variable effects of forest canopies on snow processes in a valley of the central spanish pyrenees," *Hydrol. Processes*, vol. 34, no. 10, pp. 2247–2262, 2020.

[38] T. S. Kostadinov *et al.*, "Watershed-scale mapping of fractional snow cover under conifer forest canopy using lidar," *Remote Sens. Environ.*, vol. 222, pp. 34–49, 2019.

[39] L. Baetens, C. Desjardins, and O. Hagolle, "Validation of copernicus sentinel-2 cloud masks obtained from maja, sen2cor, and fmask processors using reference cloud masks generated with a supervised active learning procedure," *Remote Sens.*, vol. 11, no. 4, 2019, Art. no. 433.

[40] O. Hagolle, M. Huc, D. VillaPascual, and G. Dedieu, "A multi-temporal and multi-spectral method to estimate aerosol optical thickness over land, for the atmospheric correction of formosat-2, landsat, ven μ s and sentinel-2 images," *Remote Sens.*, vol. 7, no. 3, pp. 2668–2691, 2015.

[41] O. Hagolle, M. Huc, C. Desjardins, S. Auer, and R. Richter, "Maja algorithm theoretical basis document," 2017. [Online]. Available: https://zenodo.org/record/1209633

[42] V. V. Salomonson and I. Appel, "Estimating fractional snow cover from modis using the normalized difference snow index," *Remote Sens. Environ.*, vol. 89, no. 3, pp. 351–360, 2004.

[43] L. P. Coons *et al.*, "Seeing the snow through the trees: Toward a validated canopy adjustment for satellite snow-covered area," *Remote Sens. Terr. Water Cycle*, vol. 206, 2014, Art. no. 199.

[44] A. Muhuri *et al.*, "Factors impacting performance of the NDSI-based operational snow cover monitoring algorithm in forested landscapes," in *Proc. EGU Gen. Assem. Conf. Abstr.*, 2021, pp. EGU 21–5139.

[45] Copernicus EU, "Pan-european high-resolution tree cover density," Accessed: Feb. 1, 2021. 2015. [*Online*]. Available: https://land.copernicus.eu/pan-european/high-resolution-layers/forests/tree-cover-density/status-maps/ 2015

[46] H. G. Jones and X. R. Sirault, "Scaling of thermal images at different spatial resolution: The mixed pixel problem," *Agronomy*, vol. 4, no. 3, pp. 380–396, 2014.

[47] A. Muhuri, "A novel perspective on mapping snow cover under forest canopy with sentinel-2 multispectral optical satellite sensor over black forest Germany," in *Proc. EGU Gen. Assem. Conf. Abstr.*, 2020, Art. no. 5617.

[48] V. V. Salomonson and I. Appel, "Development of the aqua modis NDSI fractional snow cover algorithm and validation results," *IEEE Trans. Geosci. Remote Sens.*, vol. 44, no. 7, pp. 1747–1756, Jul. 2006.

[49] L. Breiman, "Random forests," *Mach. Learn.*, vol. 45, no. 1, pp. 5–32, 2001.

[50] Y. Nakai, T. Sakamoto, T. Terajima, K. Kitamura, and T. Shirai, "Energy balance above a boreal coniferous forest: A difference in turbulent fluxes between snow-covered and snow-free canopies," *Hydrol. Processes*, vol. 13, no. 4, pp. 515–529, 1999.

[51] G. Jost, M. Weiler, D. R. Gluns, and Y. Alila, "The influence of forest and topography on snow accumulation and melt at the watershed-scale," *J. Hydrol.*, vol. 347, no. 1-2, pp. 101–115, 2007.

[52] C. R. Ellis, "Radiation and snowmelt dynamics in mountain forests," Ph.D. dissertation, Univ. Saskatchewan, Saskatoon, Canada, 2011.

[53] J. I. López-Moreno *et al.*, "The effect of slope aspect on the response of snowpack to climate warming in the pyrenees," *Theor. Appl. Climatol.*, vol. 117, no. 1-2, pp. 207–219, 2014.

[54] K. N. Musselman, J. W. Pomeroy, and T. E. Link, "Variability in shortwave irradiance caused by forest gaps: Measurements, modelling, and implications for snow energetics," *Agric. Forest Meteorol.*, vol. 207, pp. 69–82, 2015.

[55] P. Krajčí, L. Holko, and J. Parajka, "Variability of snow line elevation, snow cover area and depletion in the main slovak basins in winters2001-2014," *J. Hydrol. Hydromechanics*, vol. 64, no. 1, pp. 12–22, 2016.

[56] A. Fayad *et al.*, "Snow hydrology in mediterranean mountain regions: A review," *J. Hydrol.*, vol. 551, pp. 374–396, 2017.

[57] M. Jenicek, H. Pevna, and O. Matejka, "Canopy structure and topography effects on snow distribution at a catchment scale: Application of multivariate approaches," *J. Hydrol. Hydromechanics*, vol. 66, no. 1, pp. 43–54, 2018.

[58] M. L. Huerta, N. P. Molotch, and J. McPhee, "Snowfall interception in a deciduous nothofagus forest and implications for spatial snowpack distribution," *Hydrol. Processes*, vol. 33, no. 13, pp. 1818–1834, 2019.

[59] J. Ruiz de la Torre and L. Ceballos y Fernández de Córdoba , *Arboles y Arbustos de la España Peninsular*. Madrid, Spain: Escuela Técnica Superior de Ingenieros de Montes, 1979.

[60] J. I. López-Moreno, S. M. Vicente Serrano, E. Morán-Tejeda, J. Zabalza, J. Lorenzo-Lacruz, and J. M. García-Ruiz, "Impact of climate evolution and land use changes on water yield in the Ebro basin," *Hydrol. Earth Syst. Sci.*, vol. 15, pp. 311–322, 2011.

[61] J. D. Lundquist, S. E. Dickerson-Lange, J. A. Lutz, and N. C. Cristea, "Lower forest density enhances snow retention in regions with warmer winters: A global framework developed from plot-scale observations and modeling," *Water Resour. Res.*, vol. 49, no. 10, pp. 6356–6370, 2013.

[62] L. Korhonen, K. T. Korhonen, M. Rautiainen, and P. Stenberg, "Estimation of forest canopy cover: A comparison of field measurement techniques," *Silva Fennica*, vol. 40, no. 4, pp. 577–588, 2006.

[63] I. NSF's Division of Earth Sciences and F. Program, "National center for airborne laser mapping (NCALM)," Accessed: Feb. 1, 2021. 2016. [*Online*]. Available: http://ncalm.cive.uh.edu/

[64] M. C. Hansen *et al.*, "High-resolution global maps of 21st-century forest cover change," *Science*, vol. 342, no. 6160, pp. 850–853, 2013.

[65] T. H. Painter *et al.*, "The airborne snow observatory: Fusion of scanning lidar, imaging spectrometer, and physically-based modeling for mapping snow water equivalent and snow albedo," *Remote Sens. Environ.*, vol. 184, pp. 139–152, 2016.

[66] J. Storey, P. Scaramuzza, G. Schmidt, and J. Barsi, "Landsat 7 scan line corrector-off gap-filled product development," in *Proc. Pecora, Global Priorities Land Remote Sens.*, vol. 16, 2005, pp. 23–27.

[67] G. Yin, G. Mariethoz, Y. Sun, and M. F. McCabe, "A comparison of gap-filling approaches for landsat-7 satellite data," *Int. J. Remote Sens.*, vol. 38, no. 23, pp. 6653–6679, 2017.

[68] United States Geological Survey, "USGS earth explorer," Accessed: Feb. 1, 2021. 2021.[*Online*]. Available: https://earthexplorer.usgs.gov/

[69] D. J. Selkowitz, "Automated approaches for snow and ice cover monitoring using optical remote sensing," Ph.D. dissertation, The University of Utah, Salt Lake City, UT, USA, 2017.

[70] USGS Earth Resources Observation and Science Center, "Collection-1 landsat level-3 fractional snow covered area (FSCA) science product," Accessed: Feb. 1, 2021. 2018. [Online]. Available: https://www.usgs.gov/centers/eros/science/usgs-eros-archive-landsat-landsat-level-3-fractional-snow-covered-area-fsca

[71] J. A. Parker, R. V. Kenyon, and D. E. Troxel, "Comparison of interpolating methods for image resampling," *IEEE Trans. Med. Imag.*, vol. 2, no. 1, pp. 31–39, Mar. 1983.

[72] A. Chaponniere *et al.*, "A combined high and low spatial resolution approach for mapping snow covered areas in the atlas mountains," *Int. J. Remote Sens.*, vol. 26, no. 13, pp. 2755–2777, 2005.

[73] E. Beauxis-Aussalet and L. Hardman, "Visualization of confusion matrix for non-expert users," in *Proc. IEEE Conf. Vis. Analytics Sci. Technol. (VAST)-Poster Proc.*, 2014, p. 2.

[74] R. G. Congalton and K. Green, *Assessing the Accuracy of Remotely Sensed Data: Principles and Practices*. Boca Raton, FL, USA: CRC Press, 2019.

[75] J. Cohen, "A coefficient of agreement for nominal scales," Edu. Psychol. Meas., vol. 20, no. 1, pp. 37–46, 1960.

[76] J. R. Landis and G. G. Koch, "The measurement of observer agreement for categorical data," *Biometrics*, vol. 33, no. 1, pp. 159–174, Mar. 1977.

[77] D. N. Juurlink and A. S. Detsky, "Kappa statistic," *Can. Med. Assoc. J.*, vol. 173, no. 1, pp. 16–16, 2005.

[78] S. Gascoin *et al.*, "A snow cover climatology for the pyrenees from modis snow products," *Hydrol. Earth Syst. Sci.*, vol. 19, pp. 2337–2351, 2015.

[79] A. Rango and K. Itten, "Satellite potentials in snowcover monitoring and runoff prediction," *Hydrol. Res.*, vol. 7, no. 4, pp. 209–230, 1976.

[80] X. Wang, S. Chen, and J. Wang, "An adaptive snow identification algorithm in the forests of northeast China," *IEEE J. Sel. Topics Appl. Earth Observ. Remote Sens.*, vol. 13, pp. 5211–5222, 2020.

[81] A. G. Klein, D. K. Hall, and G. A. Riggs, "Improving snow cover mapping in forests through the use of a canopy reflectance model," *Hydrol. Processes*, vol. 12, no. 10-11, pp. 1723–1744, 1998.

[82] D. Hall, J. Foster, D. Verbyla, A. Klein, and C. Benson, "Assessment of snow-cover mapping accuracy in a variety of vegetation-cover densities in central alaska," *Remote Sens. Environ.*, vol. 66, no. 2, pp. 129–137, 1998.

[83] D. Bitner, T. Carroll, D. Cline, and P. Romanov, "An assessment of the differences between three satellite snow cover mapping techniques," *Hydrol. Processes*, vol. 16, no. 18, pp. 3723–3733, 2002.

[84] D. K. Hall and G. A. Riggs, "Accuracy assessment of the modis snow products," *Hydrol. Processes*: Int. J., vol. 21, no. 12, pp. 1534–1547, 2007.

[85] S. Metsämäki *et al.*, "Introduction to globsnow snow extent products with considerations for accuracy assessment," *Remote Sens. Environ.*, vol. 156, pp. 96–108, 2015.

[86] M. C. Serreze, M. P. Clark, R. L. Armstrong, D. A. McGinnis, and R. S. Pulwarty, "Characteristics of the western united states snowpack from snowpack telemetry (snotel) data," *Water Resour. Res.*, vol. 35, no. 7, pp. 2145–2160, 1999.

Arnab Muhuri received the Master of Technology degree in statistical modeling of multiband polarimetric synthetic aperture radar image, and the Ph.D. degree in algorithms for remote earth observation of snow cover by satellite SAR images from the Indian Institute of Technology (IIT) Bombay, Mumbai, India, in 2012 and 2018, respectively.

He was with the Microwave Remote Sensing Lab at IIT Bombay, where he researched in the domain of development of Earth observation algorithms and Lunar polar region investigations in collaboration with Defence Research and Development Organisation (DRDO), Ministry of Defence, Government of India and Indian Space Research Organisation (ISRO) respectively. He was awarded the DST-JSPS Grant in 2014 and was a Visiting Fellow at the University of Tokyo, Japan. For his research contributions, he was conferred upon the Excellence in PhD Research Award by the Honourable Prime Minister of India, Shri. Narendra Modi, at the 56th Institute Convocation of IIT Bombay in 2018. He was awarded the Alexander von Humboldt Fellowship in 2019 and the European Research Stay Grant in 2020 by the AvH Foundation, Government of the Federal Republic of Germany. He is a Post-Doctoral Fellow at the Heidelberg University and is a Visiting Scientist at the Centre d'Etudes Spatiales de la Biosphére (CESBIO) and Centre National d'Etudes Spatiales (CNES), Toulouse, France where he works with the CNES high-performance computing facility for the development and assessment of algorithms employed for large-scale satellite-based operational Earth observation.

Simon Gascoin studied earth sciences at Ecole Normale Supérieure de Lyon, France. He received the M.Sc. degree in 2005 and the Ph.D. degree in 2009 in land surface modeling and hydrology from Sorbonne University, Paris, France.

From 2009 to 2011, he was a Researcher in hydrology with Centro de Estudios Avanzados en Zonas Áridas, Chile. Since 2011, he has been a Researcher with the French National Centre for Scientific Research (CNRS), Paris, France. He is currently with Centre d'Etudes Spatiales de la Biosphère (CESBIO), Toulouse, France. His research focuses on the development and application of remote sensing products for hydrology with a particular emphasis on the snow cover in mountain regions.

Lucas Menzel studied geology at the University of Würzburg. He graduated with a degree in hydrology from the University of Freiburg, Freiburg im Breisgau, Germany, in 1989 and the Ph.D. degree from the Swiss Federal Institute of Technology (ETH), Zurich, Switzerland, in 1996, with his thesis on the simulation of evapotranspiration at the soil-vegetation-atmosphere interface.

After working as a Postdoctoral Researcher with ETH, on the generation of evapotranspiration maps for the Hydrological Atlas of Switzerland, in 1998, he joined the Potsdam Institute for Climate Impact Research (PIK), Potsdam, Germany, where he conducted intensive investigation on the simulation of future flood events in the context of climate change. Since then, he has been involved in several projects dealing with the future development of water resources in arid and semiarid regions. After working at PIK for several years, from 2004 to 2009, he was with the University of Kassel, where he was an Assistant Professor with the Center for Environmental Systems Research (CESR), leading the further development of the global water model WaterGAP. Since 2009, he has been a Full Professor in Hydrology and Climatology with Heidelberg University, Heidelberg, Germany, and since 2020, he has been the Director of the Institute of Geography. In 2017, he was a Research Fellow with the University of Waterloo, Canada.

Tihomir S. Kostadinov received the B.S. degree in biology from the University of Richmond, Richmond, VA, USA, in 2002, with minors in mathematics and computer science. He received the M.A. degree in geography and the Ph.D. degree in marine science from the University of California Santa Barbara, Santa Barbara, CA, USA, in 2005 and 2009, respectively.

His main scientific expertise is in marine bio-optics and ocean color remote sensing, focusing on satellite algorithm development, particle size distribution, and phytoplankton biogeography. He also conducts snowpack investigations in mountain forests and snow remote sensing research employing airborne lidar. He has worked on Earth's orbital Milankovitch cycles and related astronomical visualizations, including pedagogical applications. He has broad research and pedagogical interests in planetary climates and habitability, Earth system science, meteorology, climate and climate change, biogeochemistry and the carbon cycle, GNSS/GIS, paleoclimatology, botany and plant systematics, and positional astronomy. He is also interested in scientific computing and data visualization. He is currently an Assistant Professor of Geography with the California State University San Marcos, San Marcos, CA, USA.

Adrian A. Harpold received the B.S. and M.S. degrees from Virginia Tech, Blacksburg, VA, USA, in 2003 and 2005, respectively, and the Ph.D. degree from Cornell University, Ithaca, NY, USA, in 2010.

He was a Postdoctoral researcher with the University of Colorado and the University of Arizona. He is currently an Associate Professor of Mountain Ecohydrology with the University of Nevada, Reno, NY, USA. He is interested in understanding the fate and transport of water, energy, carbon, and biogeochemical solutes at the landscape scale through improved understanding of ecohydrological processes. His research threads between basic and applied science.

Juan I. López-Moreno, studied geography and received the Ph.D. from the University of Zaragoza, Zaragoza, Spain, in 2005.

His doctoral thesis dealt with the effect of climate change and forest growth on the hydrology of the Pyrenees, and how decreasing runoffs affected the dam operations for the existing reservoirs over the study area. After his Postdoctoral work at the University of Geneva, Switzerland, in 2010, he joined the Pyrenean Institute of Ecology, Zaragoza, Spain, in 2010. His research aims to understand how changes in climate and land cover affects hydrology of mountain areas with special focus on snow and glacier hydrology. His main area of focus is The Pyrenees and he also enjoys visiting other mountains around the world.

Dr. López-Moreno is the Associate Editor of *Regional Environmental Change and Atmospheric Research*.

Alba Sanmiguel-Vallelado received the B.S. degree in environmental sciences from the University of León, León, Spain, in 2013, and the M.S. degree in environmental management of water systems from the University of Cantabria, Santander, Spain, in 2015. She is currently working toward the Ph.D. degree in management of territory and natural environment at the Pyrenean Institute of Ecology, Spanish Research Council (IPE-CSIC), University of Zaragoza, Zaragoza, Spain.

She joined the IPE-CSIC in 2015, where she has been working on field data collection in high mountain environments. Her research involves snowpack dynamics in mountain forests and possible feedbacks for tree growth.